International Journal of Thermal Sciences 153 (2020) 106340

Contents lists available at ScienceDirect

International Journal of Thermal Sciences

journal homepage: http://www.elsevier.com/locate/ijts

Fluid-structure interaction of a hot flexible thin plate inside an enclosure

S.A.M. Mehryan [a], Ammar Alsabery [b,c], Alireza Modir [d], Ehsan Izadpanahi [d], Mohammad Ghalambaz [e,f,*]

[a] Young Researchers and Elite Club, Yasooj Branch, Islamic Azad University, Yasooj, Iran
[b] Refrigeration & Air-conditioning Technical Engineering Department, College of Technical Engineering, The Islamic University, Najaf, Iraq
[c] Centre for Modelling & Data Science, Faculty of Science & Technology, Universiti Kebangsaan Malaysia, 43600, UKM Bangi, Selangor, Malaysia
[d] Department of Mechanical and Material Engineering, Florida International University, Miami, FL 33174, United States
[e] Department for Management of Science and Technology Development, Ton Duc Thang University, Ho Chi Minh City, Vietnam
[f] Faculty of Applied Sciences, Ton Duc Thang University, Ho Chi Minh City, Vietnam

ARTICLE INFO

Keywords:
Arbitrary Lagrangian-Eulerian (ALE)
Fluid-structure interaction (FSI)
Inclined flexible plate
Hot plate

ABSTRACT

This study aims to assess the natural convection heat transfer in a square cavity wherein the buoyancy-induced flow is generated by a thin flexible heater-plate inside the cavity. The vertical walls of the cavity are cold and the horizontal walls are adiabatic. The thin hot plate is assumed to be isothermal and fixed at an alterable point in the middle of the cavity with different inclination angles. To analysis the fluid-structure interaction (FSI), the finite element method along with the Arbitrary Lagrangian-Eulerian (ALE) technique is employed. Isotherms and streamlines, as well as the average Nusselt number, the dimensionless temperature in the cavity, and the maximum applied stress on the flexible plate, are studied. The results are presented as a function of Rayleigh number, Prandtl number, inclination angle, and different positions of the fixed point. The outcomes indicate the importance of the inclination angle and the position of the fixed point of the hot plate. The plate experiences significantly large values of stress when it is mounted horizontally. In the case of a plate fixed at its top, the highest stress occurs with an inclination angle of 40°. In contrast, the lowest stress is associated with the plate when it is positioned vertically.

1. Introduction

Natural convection inside an enclosure has been investigated comprehensively due to its prime importance in heat transfer engineering applications such as electronic cooling [1], solar collectors [2], energy storage systems [3], and heat exchangers [4,5]. A heated fluid moves upward due to the density reduction which results in fluid circulation inside enclosed spaces [6]. Based on the entities temperature in enclosures, natural convection can be classified into two main categories. The first type occurs when the temperature difference between individual entities in the enclosure itself induces natural convection [7]. The second type is when the inner object has a different temperature with the enclosure, which results in heat transfer between the inner object and the enclosure. The inner objects influence the flow circulation in the enclosure [8,9].

Natural convection in cavities without inner objects have been widely investigated in the past decades, including the nanofluids [10], hybrid nanofluids [11], nano encapsulated phase change suspensions [12–14], and porous media [15,16]. There are also many studies regarding the boundary layer heat transfer of nanofluids [17], and nano encapsulated phase change suspensions [18]. Currently, the interest has shifted to complex cavities with internal obstacles such as complex cylinders [19] or rectangular shape obstacles [20] inside the cavities. Zhang et al. [6] numerically studied the natural convection in a circular enclosure with an inner flat plate located asymmetrically about the center of the cylinder. The surface of the enclosure was kept cold while the plate had a high temperature. Wang et al. [21] explored the natural convection in a square cavity with a vertical thin isolated plate near the walls of the enclosure for three typical Rayleigh numbers. They studied the effect of the inner plate position and found a good agreement between their numerical results with the flow visualization.

Altac and Kurtul [8] numerically studied the natural convection in a tilted rectangular cavity, containing a vertical thin isothermal hot plate. The tilt angle and Rayleigh numbers were in the range of 0°–90° and 10^5 to 10^7, respectively. The results showed an increase in the average

* Corresponding author. Ton Duc Thang University, Ho Chi Minh City, Vietnam.
E-mail addresses: alal171366244@gmail.com (S.A.M. Mehryan), ammar_e_2011@yahoo.com (A. Alsabery), eizad001@fiu.edu (E. Izadpanahi), mohammad.ghalambaz@tdtu.edu.vn (M. Ghalambaz).

https://doi.org/10.1016/j.ijthermalsci.2020.106340
Received 26 July 2019; Received in revised form 18 February 2020; Accepted 19 February 2020
Available online 5 March 2020

Nomenclature

Latin symbols

$\boldsymbol{d}_s$	Solid displacement vector
E	Dimensionless elasticity modulus
E_τ	Young's modulus
$\mathbf{F}v$	Dimensionless body force
g	Gravitational acceleration
l	Plate length
L	Cavity size
Nu	Nusselt number
Pr	Prandtl number
P_1, P_2, P_3	Fixed points
Ra	Rayleigh number
t	Time
t_p	Thin plate thickness
T	Temperature
$\boldsymbol{u}$	Fluid velocity vector
$\boldsymbol{W}$	Moving coordinate velocity
x, y	Cartesian coordinates

Greek symbols

α	Thermal diffusivity
β	Thermal expansion coefficient of fluid
γ	Inclination angle
υ_f	Kinematic viscosity
ρ	Density
$\boldsymbol{\sigma}$	Stress tensor
τ	Dimensionless time

Subscripts

c	Cold
f	Fluid
h	Hot
p	Plate
R	Property ratio of the solid to the fluid
s	Solid

Superscripts

*	Dimensional parameters

Nusselt number with raise of the tilt angles up to 22.5°, and then, it decreased for all Ra numbers. Shi and Khodadadi [22] investigated the effect of a conductive thin fin on the wall of a square cavity at seven different locations and different aspect ratios.

In fluid-structure interaction (FSI) problems, the interaction of a moving or deformable structure with a surrounding or internal fluid flow is studied. FSI occurs in many physical phenomena and has wide applications in engineering problems such as ocean energy converters [23,24], airplane wings stability [25], and wind turbine blades [26]. Due to the vital importance and broad application of FSI in engineering problems and especially in heat transfer, it has received significant attention in recent years.

Considering natural convection inside enclosures, the effects of fluid-structure interaction on the heat transfer rate and flow domain have been investigated in limited studies [27–32]. The complexity of the physics and time-consuming nature of calculations, as well as the limitation of computational hardware in the past, made the numerical analysis of these problems inconvenient. The effect of thermal buoyancy on the vortex-induced vibration (VIV) of a flexible mounted circular cylinder is numerically investigated in Ref. [33]. Thermal control as a method for VIV suppression is implemented in Ref. [34]. Fluid-solid interaction in a cavity has been studied in two main cases when one or more walls of the enclosure considered to be flexible [35,36] or existence of a flexible membrane or plates inside the enclosure that influence the heat transfer and fluid behavior in the cavity [28,37,38]. Different industrial applications can be mentioned for these two configurations, such as enclosures with an internal electronic board or enclosures which employed thermal conductive plates for partitioning different electronic units [36]. Chemical reactors or batteries, where plates and membranes should separate different chemical fluids, can be considered as another industrial application of fluid-solid interaction in a cavity [28].

The comparisons of the average Nusselt number of the flexible walls and rigid walls in the enclosure in Refs. [35,36] confirm the significant effect of the flexible walls on the heat transfer rate inside a cavity. Al-Amiri and Khanafer [35] reported a 9.4% difference between the Nusselt number of a cavity with a rigid bottom wall and a cavity with a flexible bottom wall, which is a function of Reynolds number and

Table 1
Literature review summary of the natural convection heat transfer in an enclosure.

Reference	Type of enclosure	Inner Object	Studied parameter	Method
[9]	Square	Corrugated conducting block	Entropy generation	FVM
[10]	Elliptic	elliptic	Nanofluids	FVM
[8]	Tilted square	Plate	Tilt angle and Ra Number	FVM
[11]	Square	Rectangle	Hybrid nanofluid	FEM
[12,13]	Square	–	Nano-Encapsulated Phase Change Materials suspension	FEM
[14]	Circle	Circle	Location of inner circle	FEM
[15]	Square	–	Porous media and location of heated boundaries	FEM
[16]	Incinerator shape	Rectangular wavy heater block	Magnetic field and Rayleigh number	FVM
[19]	Square	Wavy circular heater	Magnetic field and Rayleigh number	Control Volume-FEM
[20]	Square	Square	Nanofluids and porous media	FDM
[21]	Square	Plate	Plate location near walls	FVM
[22]	Square	Porous fin	Fin inclination angle and location	FEM
[28,29]	Square	Thin flexible partition	Flexibility of the partition	FEM
[30,31]	Square	Circle	Flexibility of wall	FEM
[32]	Square	Flexible fin	Oscillation of flexible fins	
[27,35]	Lid driven square cavity	Flexible bottom wall	Profile of the flexible bottom wall	FEM- FSI
[36]	Square-Filled with porous medium	Flexible vertical wall	Porosity, elasticity of the flexible wall	FEM-FSI
[28]	Square cavity divided into two triangle part	Flexible diagonal membrane	Stiffness of the membrane	FEM-FSI
[37]	Square	Oscillating Elastic fin	Oscillation amplitude and frequency	FEM-FSI
[38]	Square	Flexible vertical membrane	Magnetic field orientation	FEM-FSI
[39]	Square	Hot flexible plate	The elasticity modulus, the height and length of the plate.	FEM-FSI

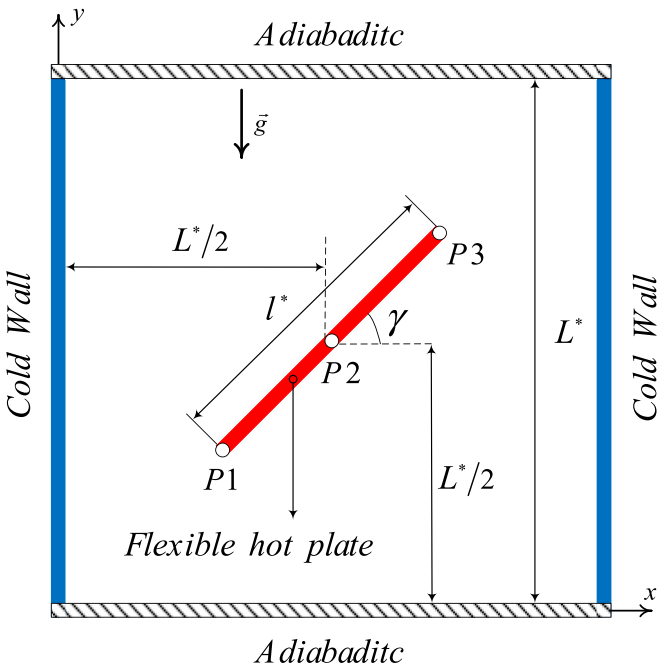

Fig. 1. A schematic of the physical model.

Table 2
Grid testing for $\overline{Nu}$, σ_{max} and T at different grid sizes for fixed point 1 ($P1$), $Ra = 10^6$, $\gamma = 90°$ and $Pr = 6.2$.

Grid size	Number of elements (Fluid domain)	Number of elements (Flexible plate)	$\overline{Nu}$	σ_{max}	T
G1	2274	72	14.038	5.76E+08	0.33515
G2	2490	72	14.146	5.77E+08	0.33527
G3	2830	72	14.149	5.78E+08	0.33532
G4	3444	72	14.154	5.81E+08	0.33554
G5	3810	69	14.155	5.82E+08	0.3356
G6	5423	89	14.155	5.82E+08	0.3356
G7	5687	99	14.156	5.82E+08	0.3358
G8	7145	223	14.157	5.83E+08	0.3355

increases by increasing Reynolds number. In the case of free convection with a flexible sidewall which was reported in Ref. [36], the maximum Nusselt number of the cavity increased 13.6% in comparison with the case of rigid sidewalls. It was also reported that the flexibility of the sidewall improves the Nusselt number and heat transfer rate. Hence, the heat transfer rate in a cavity with a flexible sidewall is better than a

Table 3
Properties of the fluid and flexible wall of the Küttler and Wall's problem [52].

Properties	Flexible wall	Fluid
Kinematic viscosity (υ_f)	–	0.01 m^2/s
Density (ρ)	500 kg/m^3	1 kg/m^3
Poisson's ratio (ν_s)	0.0	–
Young's modulus (E_τ)	250 N/m^2	–
Thickness	0.002 m	–

cavity with rigid walls. In the case of natural convection in enclosures with flexible partitions [28,29,38], flexible walls [30,31], or flexible fins [37,39], the heat transfer rate enhanced when the flexibility of the partitions or fins increased. An augmentation in the flexibility of the membrane increases its deformation following the flow pattern, which leads to a considerable rise in the heat transfer inside the cavity. On the other hand, a more rigid partition creates resistance to the flow movement and consequently, declines the heat transfer rate.

Most of the studies available in the literature only have focused on vertical or horizontal rigid partitions in heat transfer applications, while in various real-world situations, the inner plate can be flexible. A summary of the heat transfer studies in a cavity with inner objects or flexible walls is presented in Table 1. Flexible heat spreader for cooling of electronic components [40,41], flexible heat exchangers for medical

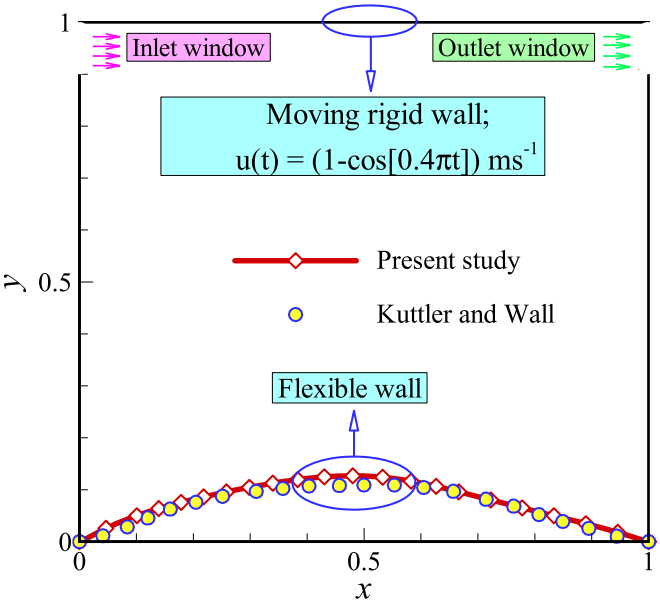

Fig. 3. A comparison between the results of the present study and [52].

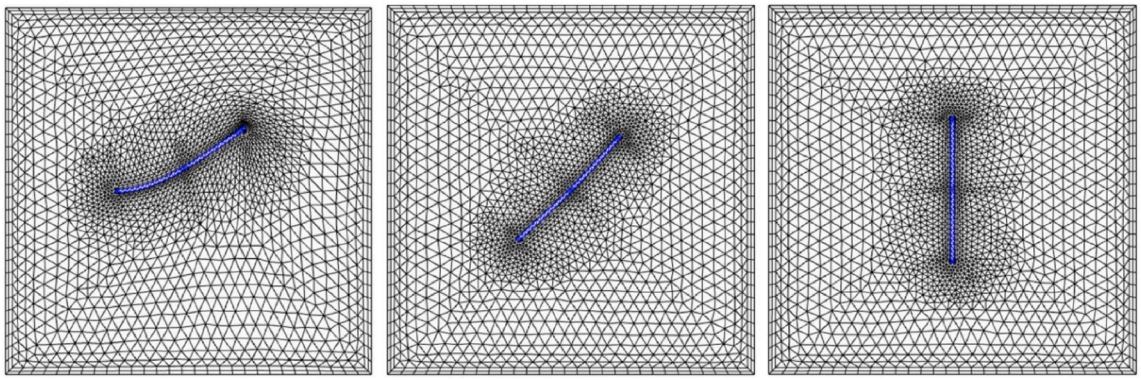

Fig. 2. Grid-points distribution for a grid size G5 = 3879 elements.

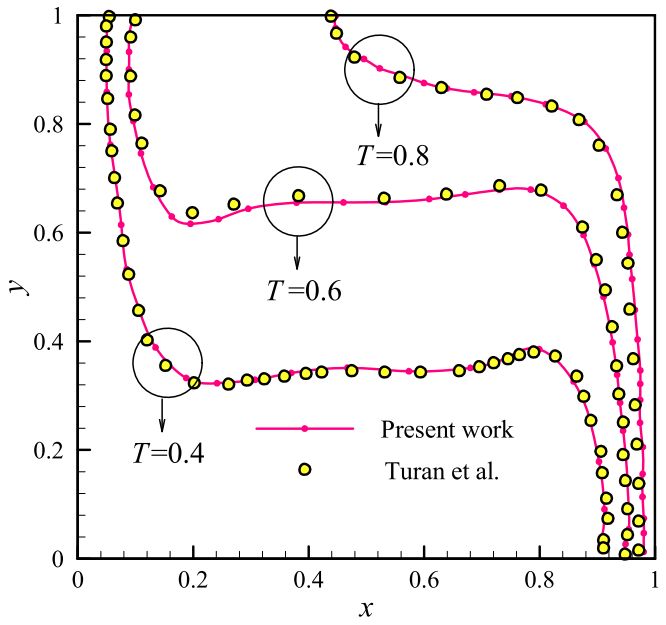

Fig. 4. A comparison of the temperature field from work conducted by Turan et al. [53] and the present prediction.

warming and cooling applications [42], and mechanically conformable micro-heat exchangers [43] are examples of such systems.

The flexibility of the internal partition affects the heat transfer and flow inside the enclosure which requires the analysis of the fluid-structure interaction for calculating the heat transfer and studying the geometry of the partition. In our previous study [39], the effect of the flexibility of a thin plate on the natural convection heat transfer was addressed while the plate was mounted horizontally and fixed at its center. In Ref. [39] we focused on the flexibility of the plate fixed at its center to study the heat transfer and induced stresses in it. In Ref. [39], we learned that the flexibility and interaction between the fluid and structure notably affect the thermal behavior of the cavity and the induced stresses in the plate. However, not only the flexibility of the plate (addressed in Ref. [34]) but also the clamping location of the plate

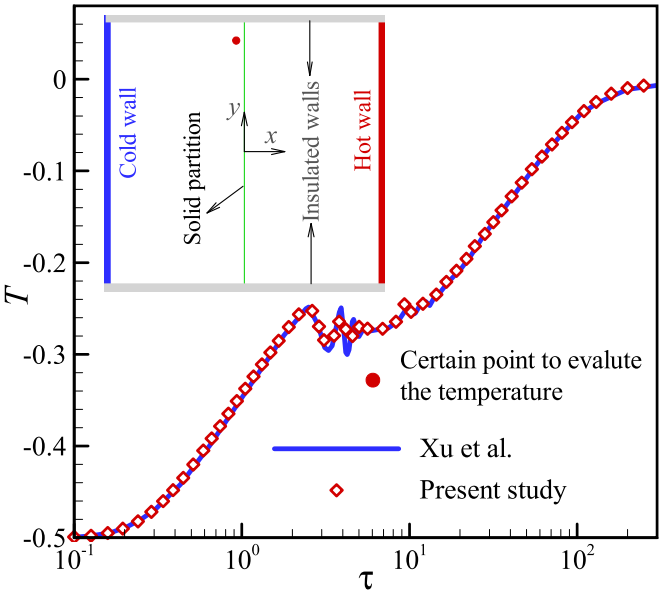

Fig. 5. The time history of the non-dimensional temperature at the denoted point for the present work and [54].

(the mechanical boundary condition for fixing of the plate) and the mounting angle of a plate could be important parameters on the thermal and mechanical behavior of the cavity and the baffle.

To the best of authors' knowledge, the effect of the inclination angle of a flexible hot plate on the natural heat transfer inside a cavity has not been addressed before. In this study, a comprehensive numerical investigation is provided on natural convection heat transfer in a square cavity containing an internal flexible hot thin-plate. The plate is fixed at three different locations in a wide range of inclination angles to assess the effects of the flexibility of the plate and the location of the fixed point on the heat transfer and flow characteristics.

2. Problem definition and mathematics

A square 2D enclosure with an inclined flexible plate, shown in Fig. 1, is considered as the geometry of the study. The vertical bounds of the square, having the length of L^*, are kept at the constant temperature of T_c^*, and the horizontal walls are adiabatic. The thin heater plate has the thickness of t_p^* and is isothermal with the higher temperature of T_h^*. The inclination angle of the plate with respect to the horizontal line is considered as γ.

All of the solid walls of the cavity and the walls of the flexible plate are impervious against the mass diffusion. The flexible heater can be fixed at one of the three points depicted in Fig. 1 ($P1$, $P2$ or $P3$). The flow of the fluid inside the enclosure is simulated as laminar, incompressible and Newtonian.

The governing equations are introduced in Ref. [39] and can be transformed into a non-dimensional form by considering the cavity size as the characteristic length, and α_f/L^* as a reference with the same dimension as the velocity. The governing equations of [39] can be transformed into a non-dimensionalized form by utilizing the non-dimensional varying parameters presented below:

$$\mathbf{d}_s = \frac{\mathbf{d}_s^*}{L^*},\ \boldsymbol{\sigma} = \frac{\boldsymbol{\sigma}^*}{E_\tau},\ \tau = \frac{t\alpha_f}{L^{*2}},\ (x, y, l, t_P) = \frac{(x^*, y^*, l^*, t_P^*)}{L^*}, \mathbf{u} = \frac{\mathbf{u}^* L^*}{\alpha_f},\ \mathbf{w} = \frac{\mathbf{w}^* L^*}{\alpha_f},\ P = \frac{P^* L^{*2}}{\rho_f \alpha_f^2},\ T = \frac{T^* - T_c^*}{T_h^* - T_c^*} \tag{1}$$

where the fluid velocity vector and the moving coordinate velocity are denoted as $\boldsymbol{u}^*$ and $\boldsymbol{w}^*$, respectively. Fluid pressure and the fluid/solid temperature are denoted as P^* and T^*, respectively. Here, the density is ρ and thermal diffusivity is α_f. The subscripts f and s represent the fluid and the solid. The tensor and vector fields are denoted in bold.

The non-dimensional equations describing the thermal and dynamic behavior of the fluid in the Arbitrary Lagrangian-Eulerian (ALE) formulation are listed below:

$$\nabla \cdot \mathbf{u} = 0 \tag{2}$$

$$\frac{\partial \mathbf{u}}{\partial \tau} + (\mathbf{u} - \mathbf{w}) \cdot \nabla \mathbf{u} + \nabla P - Pr\nabla^2 \mathbf{u} - PrRaT\mathbf{j} = 0 \tag{3}$$

$$\frac{\partial T}{\partial \tau} + (\mathbf{u} - \mathbf{w}) \cdot \nabla T - \nabla^2 T = 0 \tag{4}$$

The governing non-dimensional equations for the energy and structural displacement of the flexible thin plate can be expressed as equation (5). Here, $\boldsymbol{\sigma}$, $\boldsymbol{d}_s$, and $\boldsymbol{F}_v$ are denoted as the stress tensor, the solid displacement vector, and the applied body force, respectively.

$$\frac{d^2 \mathbf{d}_s}{d\tau^2} - \rho_R E \nabla \boldsymbol{\sigma} - \rho_R E\ \mathbf{F}_v = 0 \tag{5}$$

The non-dimensional constant parameters that appeared above are as follows:

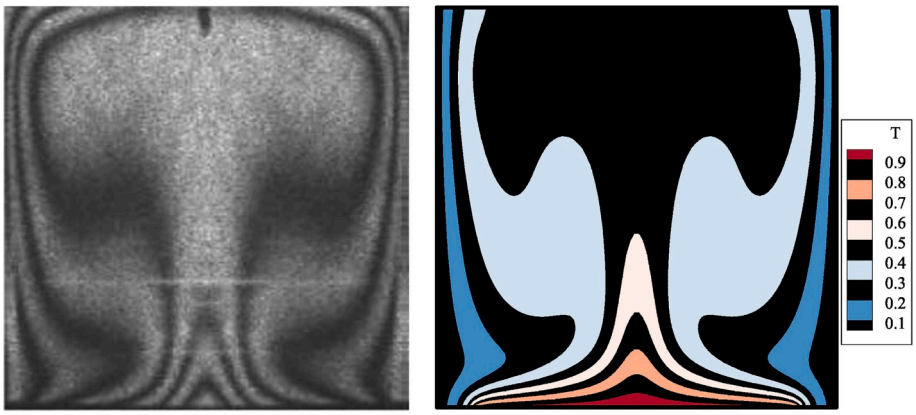

Fig. 6. A comparison between the temperature fields of (a): the current numerical study and (b): the experimental work performed by Calcagni et al. [55].

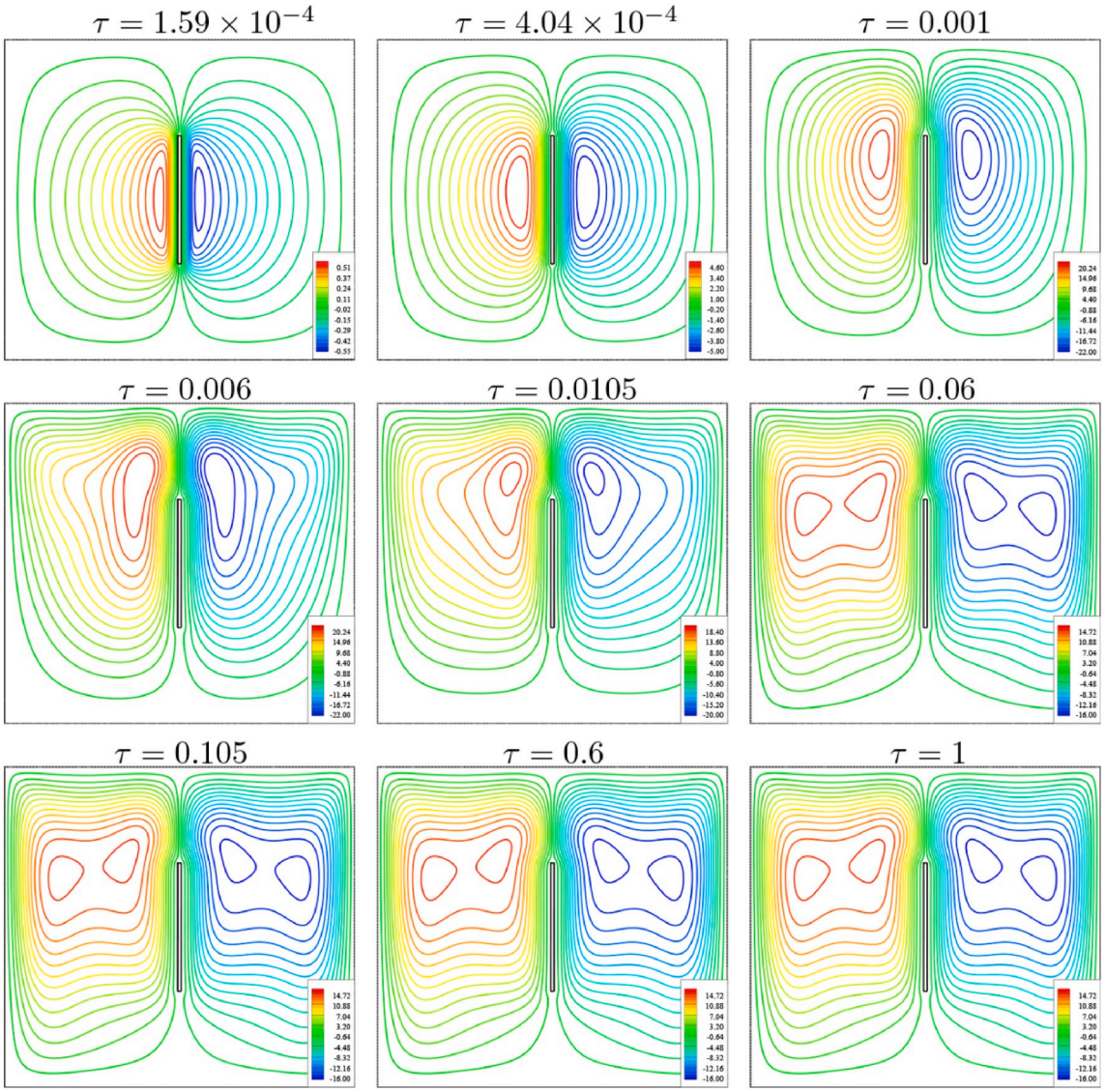

Fig. 7. Variations of the unsteady streamlines for various dimensionless time (τ) at fixed point 1 ($P1$), $Ra = 10^6$, $\gamma = 90^\circ$, $Pr = 6.2$, and $E = 5 \times 10^{10}$.

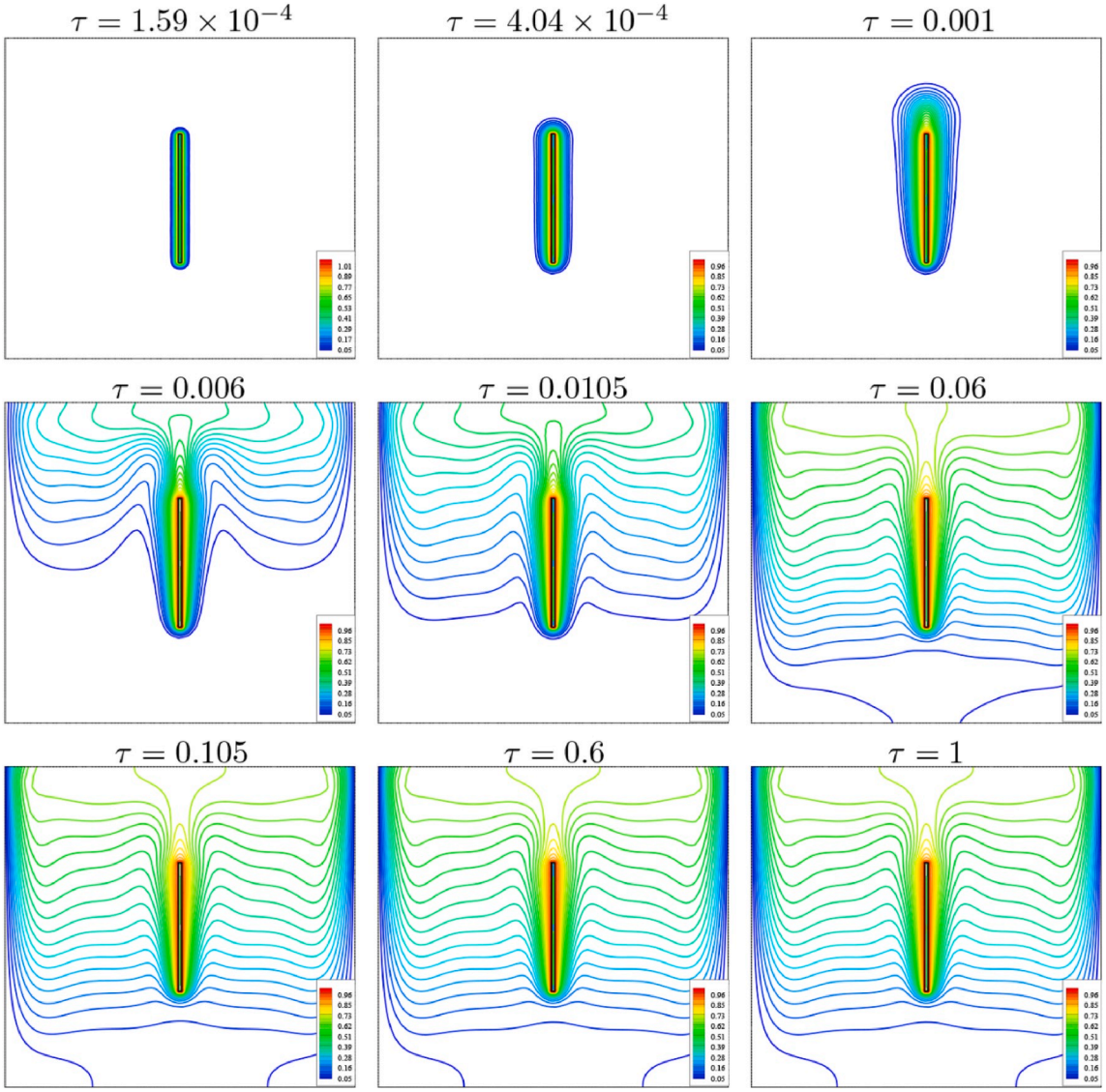

Fig. 8. Variations of the unsteady isotherms for various dimensionless time (τ) at fixed point 1 (*P*1), $Ra = 10^6$, $\gamma = 90°$, $Pr = 6.2$, and $E = 5 \times 10^{10}$.

$$Ra = \frac{g\beta\left(T_h^* - T_c^*\right)L^{*3}}{\upsilon_f \alpha_f}, \quad Pr = \frac{\upsilon_f}{\alpha_f}, E = \frac{E_\tau L^{*2}}{\rho_f \alpha_f^2}, \quad \mathbf{F}_v = \frac{\left(\rho_f - \rho_s\right)L^* \mathbf{g}}{E_\tau}, \quad \rho_R = \frac{\rho_f}{\rho_s} \tag{6}$$

where ν_f is the kinematic viscosity of the fluid, β is the volumetric thermal expansion coefficient, and $\boldsymbol{g}$ is the gravitational acceleration. Here, it is assumed that $\rho_f = \rho_s$. Therefore, $\rho_R = 1$ and $\boldsymbol{F}_v = 0$.

Taking into consideration the no-slip condition in the interface of the fluid at the solid, the boundary conditions in the dimensionless coordinates can be referred to below:

At the surfaces of the flexible plate:

$$T = 1, \quad \frac{\partial \mathbf{d}_s}{\partial t} = \mathbf{u}, \quad \boldsymbol{\sigma} \cdot n = -P + \mu_f \nabla \mathbf{u} \tag{7-a}$$

At the vertical walls:

$$T = 0, \quad u = v = 0 \tag{7-b}$$

At the horizontal walls:

$$\frac{\partial T}{\partial y} = 0, \quad u = v = 0 \tag{7-c}$$

The points *P*1–*P*3 are fixed points with zero solid-velocity at both x and y directions as:

$$\frac{\partial \mathbf{d}_s}{\partial t} = 0 \tag{7-d}$$

At the beginning of the natural convection, the fluid is motionless, and its temperature is the average of the thin plate (T_h^*) and cold temperatures of vertical walls (T_c^*). The physical coupling of the fluid domain and the structure (plate) is through the boundary condition of Eq. (7-a). The fluid interacts with the plate through the surface forces and induces tensions in the plate. The induced tensions in the plate lead to the deformation of the plate. Consequently, the plate deformation changes the geometry of the plate and affects fluid hydrodynamic and heat transfer. As the interaction of the fluid, heat transfer, and the structure are fully coupled, any changes in the hydrodynamic, heat transfer or the structure would affect all of the physics and equations, simultaneously.

To measure the heat transfer rate through the flexible heater, the average Nusselt number is defined as Eq. (8) where n and s are respectively the normal-direction and the tangential-direction with the surface of the flexible plate.

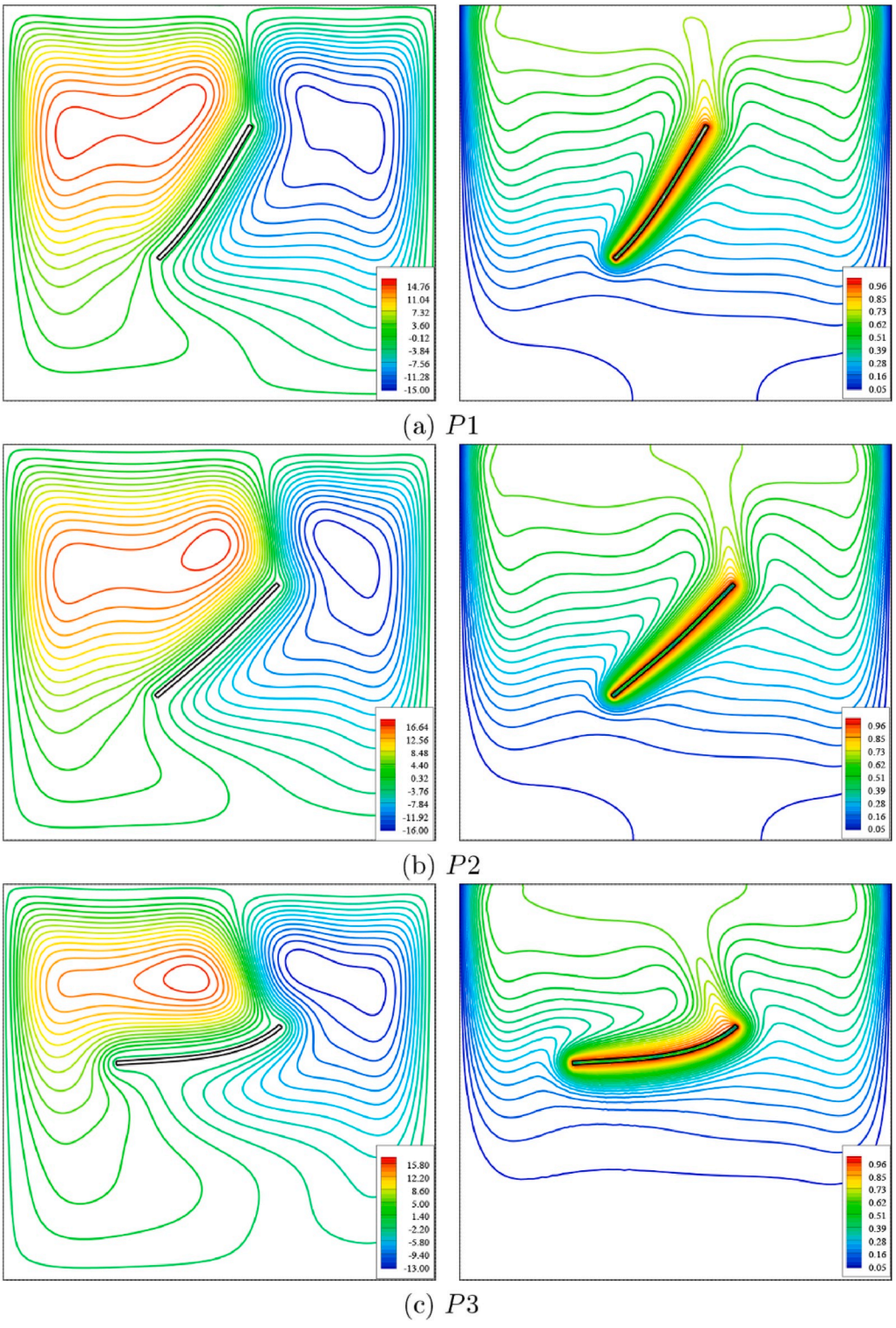

Fig. 9. Variations of the steady streamlines and isotherms for various fixed point locations ($P1$–$P3$) at $Ra = 10^6$, $\gamma = 45^\circ$, $Pr = 6.2$, and $E = 5 \times 10^{10}$.

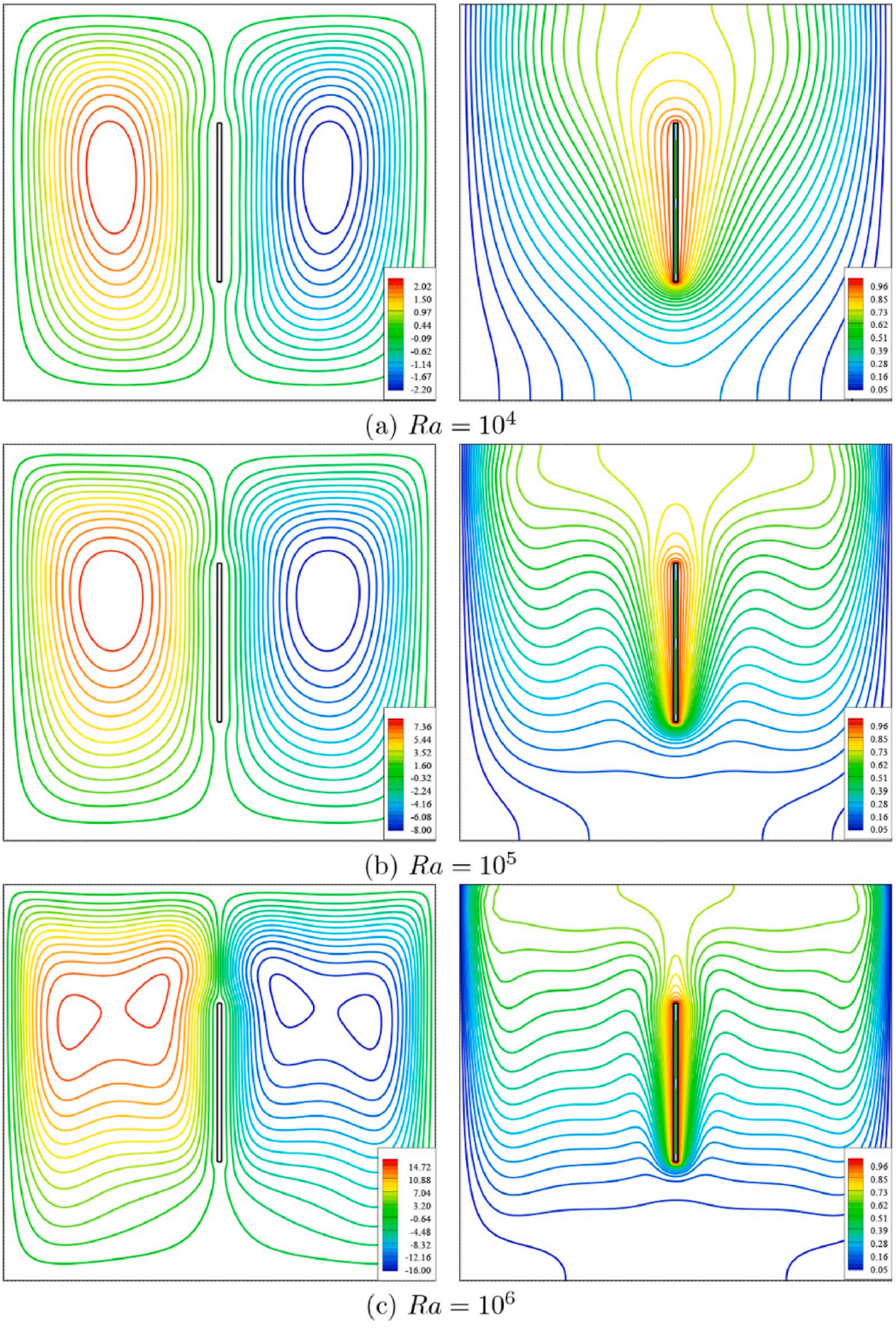

Fig. 10. Variations of the steady streamlines and isotherms for various Rayleigh number (Ra) at fixed point 1 ($P1$), $\gamma = 90^\circ$, $Pr = 6.2$, and $E = 5 \times 10^{10}$.

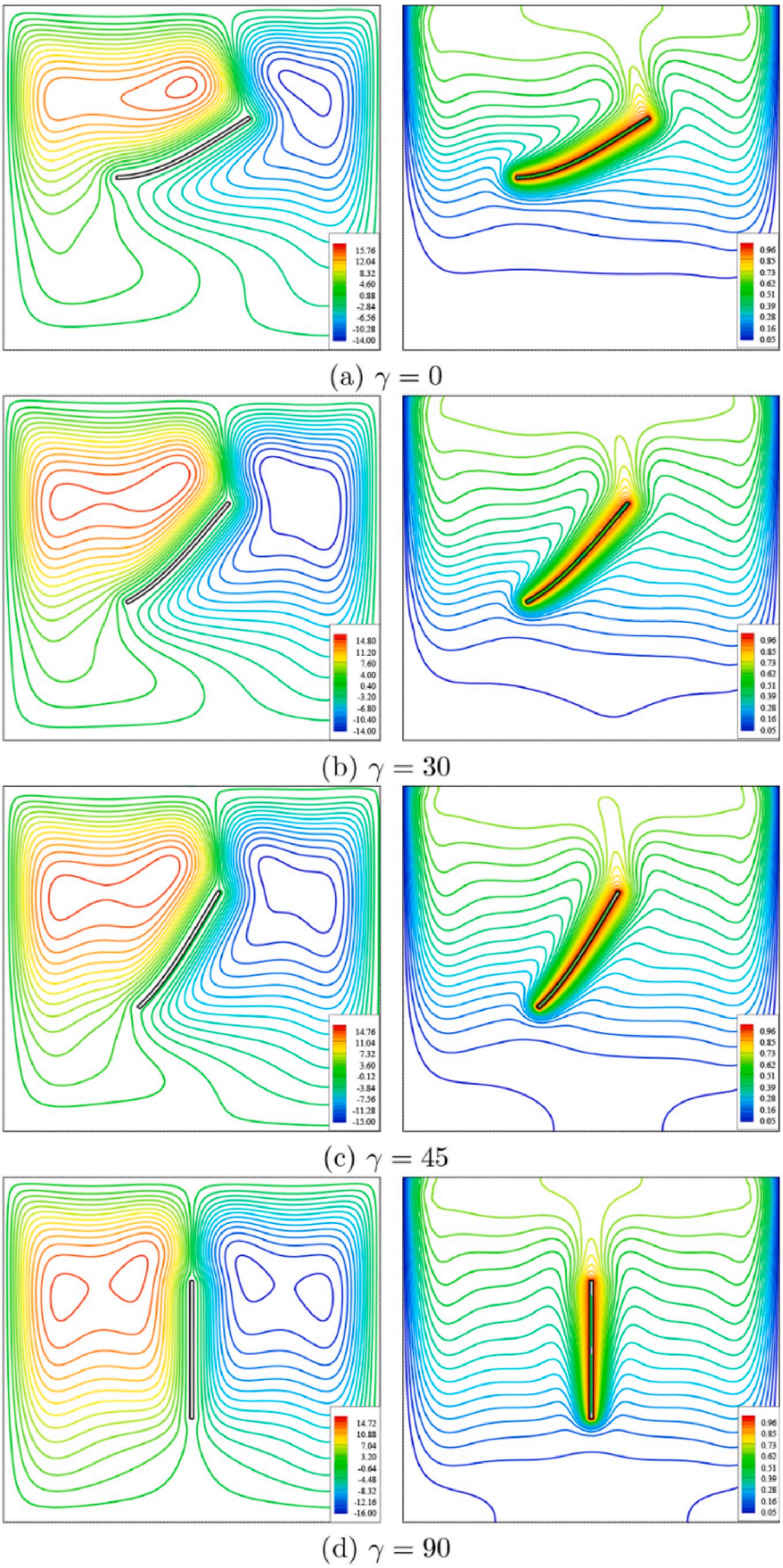

Fig. 11. Variations of the steady streamlines and isotherms for various angles of the flexible heated plate (γ) at fixed point 1 ($P1$), $Ra = 10^6$, $Pr = 6.2$ and $E = 5 \times 10^{10}$.

$$\overline{Nu} = -\frac{1}{2\,(l+t_P)} \int_{Hot\ \ plate} \left.\frac{\partial T}{\partial n}\right|_{On\ \ the\ \ hot\ \ plate} ds \tag{8}$$

3. Numerical solution, grid independence test, and verifications

3.1. Numerical solution

The governing equations, Eqs. (2)–(5), with the stated boundary conditions, are numerically solved. Due to the fluid-solid interaction inside the cavity and heat transfer at the interface of fin and fluid, a finer grid is utilized at the boundary interfaces to increase the numerical accuracy of the solution. Arbitrary Lagrangian-Eulerian (ALE) method is employed to model the motion of structure in the fluid domain [44]. The governing equations are first written in a weak form and then integrated over the domain of solution to produce the residual equations. Then, the residual equations are iteratively solved by the Newton method utilizing a PARallel DIrect SOlver (PARDISO) [45–47] with a Newtonian damping factor of 0.8 and a residual error O (10^{-6}). This method is discussed in detail in the early works of [48,49], and recent works of [50,51].

3.2. Grid independence test

Grid-independence tests are performed to ensure that the results are independent of the number of mesh elements. For this purpose, the $\overline{Nu}$, σ_{max} and T for pint 1 ($P1$) at $Ra = 10^6$, $\gamma = 90^\circ$ and $Pr = 6.2$ are examined for five different mesh sizes. The number of utilized elements for the fluid domain and the structure domain (flexible plate) are reported in Table 2 for various mesh sizes. The results, which are tabulated in Table 2, confirm that the grid size of case 5 (G5) is the most suitable mesh considering the precision and computing time. Hence the mesh of case 5 with 3879 elements is selected throughout this research. Grid-points and elements-distribution are shown in Fig. 2 for different fixed points of case 5.

3.3. Verification

Comparisons with the selective results of the available literature are conducted to check the verification of the utilized numerical methodology and the modeling. As a validation of the FSI code, Küttler and Wall's study [52] has been investigated. They considered a lid-driven square cavity with a flexible bottom wall. The top wall of the cavity was driven at a velocity of $(1-\cos(0.4\pi t))$ m/s. On the other hand, two free openings were placed at top of the vertical walls. Horizontal oscillation of the lid excites the fluids and inside the enclosure and induces a vortex. As a result, the interaction between the fluid and flexible lower wall alters the shape of the bottom. This change in the shape of the flexible bottom wall was computed over time. Table 3 reports the thermophysical properties of flexible wall and the fluid inside the cavity, which were employed in Ref. [52]. Fig. 3 depicts a comparison of the results of the current work with [52] for the flexible wall's deformation after $t = 7.5\ s$. The comparison shows that there is a desirable agreement between the results.

To validate the natural convection heat transfer in the cavity, the study of Turan et al. [53] has been investigated. Turan et al. [53] studied the free heat transfer in a square cavity with the top and bottom insulated walls while the right and the left walls were at hot and cold temperatures. For a case of Newtonian fluid with $Pr = 1000$ and $Ra = 10^5$, a comparison between the isotherms of the present study and those of [53] is reported in Fig. 4. As it can be observed, the results are in excellent agreement.

As a transient heat transfer case, a comparison between the results of the present study and Xu et al. [54] are depicted in Fig. 5. The schematic of the studied problem by Xu et al. [54] is illustrated clearly in Fig. 5. As specified in Fig. 5, the dimensionless temperature at a certain point ($x = 0.0083$ and $y = 0.375$, assuming the coordinate system at the center of the enclosure) is selected for the comparison. The results computed in the present work are compared with the results given in Ref. [54] for a case when $Ra = 9.2 \times 10^8$ and $Pr = 6.63$. As shown in Fig. 5, the results of the current work are in good agreement with Xu et al. [54]. The present study is further validated through a comparison between its temperature field and the temperature field reported in the experimental work conducted by Calcagni et al. [55]. Calcagni et al. [55] experimentally studied an enclosure filled by air in which the horizontal walls were isothermally cooled by means of circulating thermostatic liquid. The upper wall was adiabatic and the bottom of the enclosure was partially maintained at a constant high temperature using a thermostatic bath. In this comparison, $Ra = 1.836 \times 10^5$ and $Pr = 0.71$. The matching observed in Fig. 6 between the results of current work and Calcagni et al. [55] confirms the correctness of the present solution. According to the conducted verifications, the provided code can confidently be used to reach the correct and accurate results.

4. Results and discussion

In the current section, the streamlines, isotherms, average Nusselt number, maximum stress on the flexible plate, and average dimensionless temperature are presented for different cases. The considered non-dimensional parameters in this study are as follows: fixed point location ($P1$ (fixed point 1), $P2$ (fixed point 2), $P3$ (fixed point 3)), Rayleigh number ($10^3 \le Ra \le 10^6$), the inclination angle of the flexible heated plate ($0^\circ \le \gamma \le 90^\circ$), Prandtl number ($Pr = 0.71$ (air), 6.2 (water) and 13.4 (seawater)), and the flexible plate stiffness (elasticity modulus) ($10^9 \le E \le 10^{14}$). Other parameters such as non-dimensional body force ($\boldsymbol{F}_v = 0$), the density ratio ($\rho_R = 1$), and the plate thickness ($t_P = 0.01$) remained unchanged in all simulations.

Fig. 7 shows the streamlines when the plate is fixed at $P1$ for $Ra = 10^6$, $\gamma = 90^\circ$, $Pr = 6.2$ and $E = 5 \times 10^{10}$ at different dimensionless time steps. The fluid motion reaches a steady-state condition at $\tau = 0.06$. Due to the temperature difference of the vertical walls of the cavity and the inner plate, a clockwise vortex and a counterclockwise vortex are formed in the right and the left sides of the cavity, respectively. At low values of time, the density of streamlines is high in vicinity of the hot plate compared with the other regions, indicating the start of the fluid flow ($\tau \le 10^{-3}$). At $\tau = 6 \times 10^{-3}$ the streamlines gained strength, and the cells moved toward the top wall of the cavity. The buoyancy-induced flow strengthens as time elapses. As time evolves to $\tau = 0.06$, streamlines get a double-eye circulation motion on each side of the enclosure. From $\tau = 0.06$ to $\tau = 1$, the streamlines do not experience a noticeable change which can be considered as the steady-state condition of the fluid flow.

Fig. 8 illustrates the transient development of the isothermal contours of the fluid for the same parameters of Fig. 7 at different time steps. Initially, at $\tau = 1.59 \times 10^{-4}$, pure conduction occurs around the plate. At $\tau = 0.001$, buoyancy induced flow starts to transfer heat from the plate to the medium above the plate. The isotherms distributed moderately in the upper section of the enclosure at dimensionless time $\tau = 0.006$. At $\tau = 0.0105$, isotherms are starting to align in a horizontal form and fully develop as time passes. At higher time steps, dense isotherms can be observed close to the hot plate and vertical walls. Fig. 8 indicates that at the steady-state situation, the isotherms compress and extend vertically close to vertical walls and the hot plate in the cavity.

Fig. 9 shows the steady-state contours of isotherms and streamlines for various fixed points when $\gamma = 45^\circ$, $Ra = 10^6$, $Pr = 6.2$ and $E = 5 \times 10^{10}$. The flexible hot plate experiences a substantial deformation when the fixed point is $P3$. This is caused by the buoyancy force exerted at the free bottom of the plate. It can be seen that the heater has the least deformation for the fixed point $P2$. The deformation of the plate leads to a change in the pattern of the streamlines and consequently, the heat transfer. The horizontal isotherms in the cavity indicate that the convection is the main heat transfer mechanism in the middle part of the cavity.

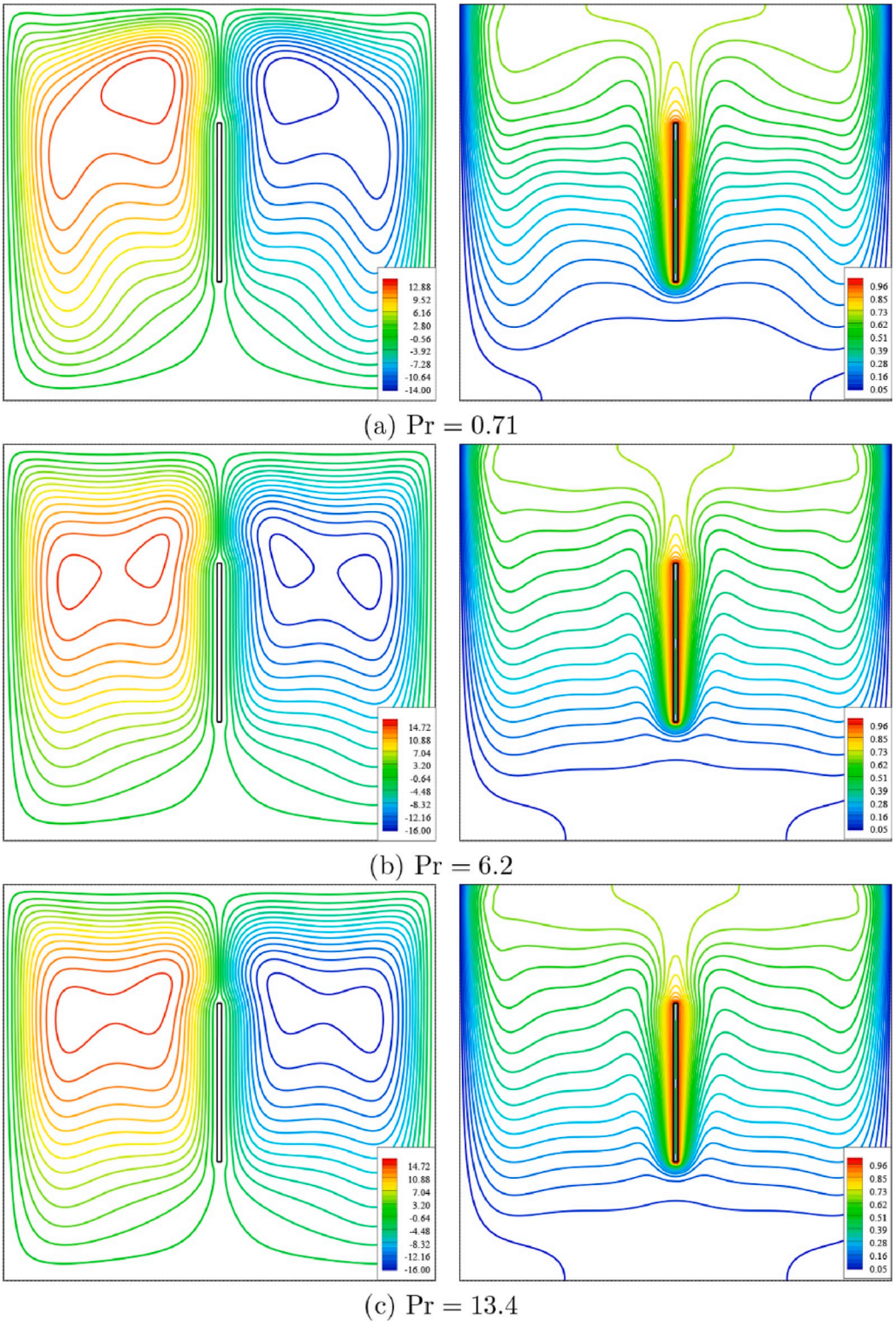

Fig. 12. Variations of the steady streamlines and isotherms for various Prandtl number (*Pr*) at fixed point 1 (*P*1), $Ra = 10^6$, $\gamma = 90^\circ$ and $E = 5 \times 10^{10}$.

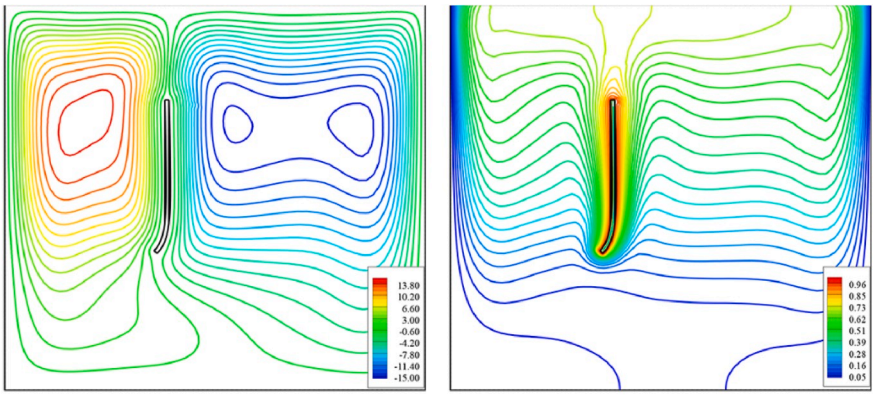

(a) $E = 10^9$

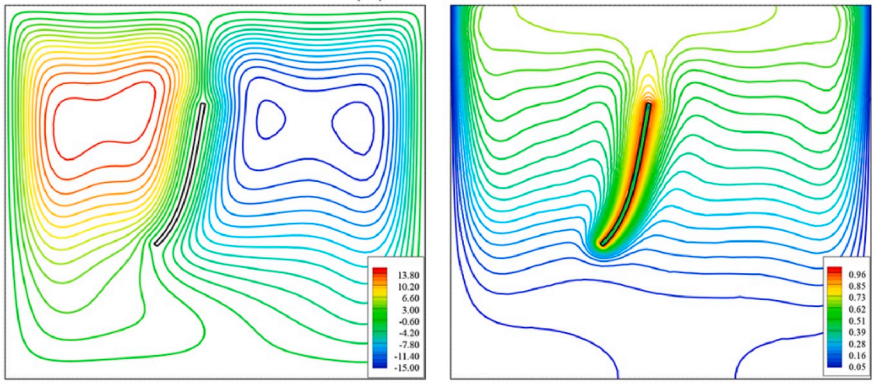

(b) $E = 10^{10}$

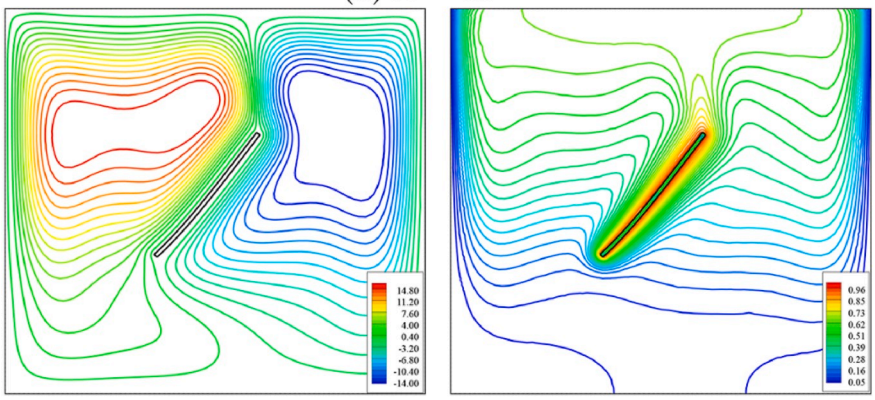

(c) $E = 10^{11}$

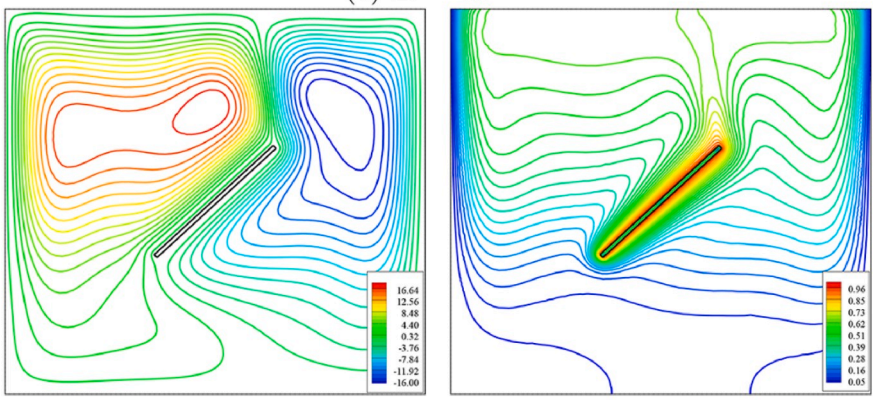

(d) $E = 10^{13}$

Fig. 13. Variations of the steady streamlines and isotherms for various elasticity modulus (E) at fixed point 1 ($P1$), $Ra = 10^6$, $\gamma = 45^\circ$ and $Pr = 6.2$.

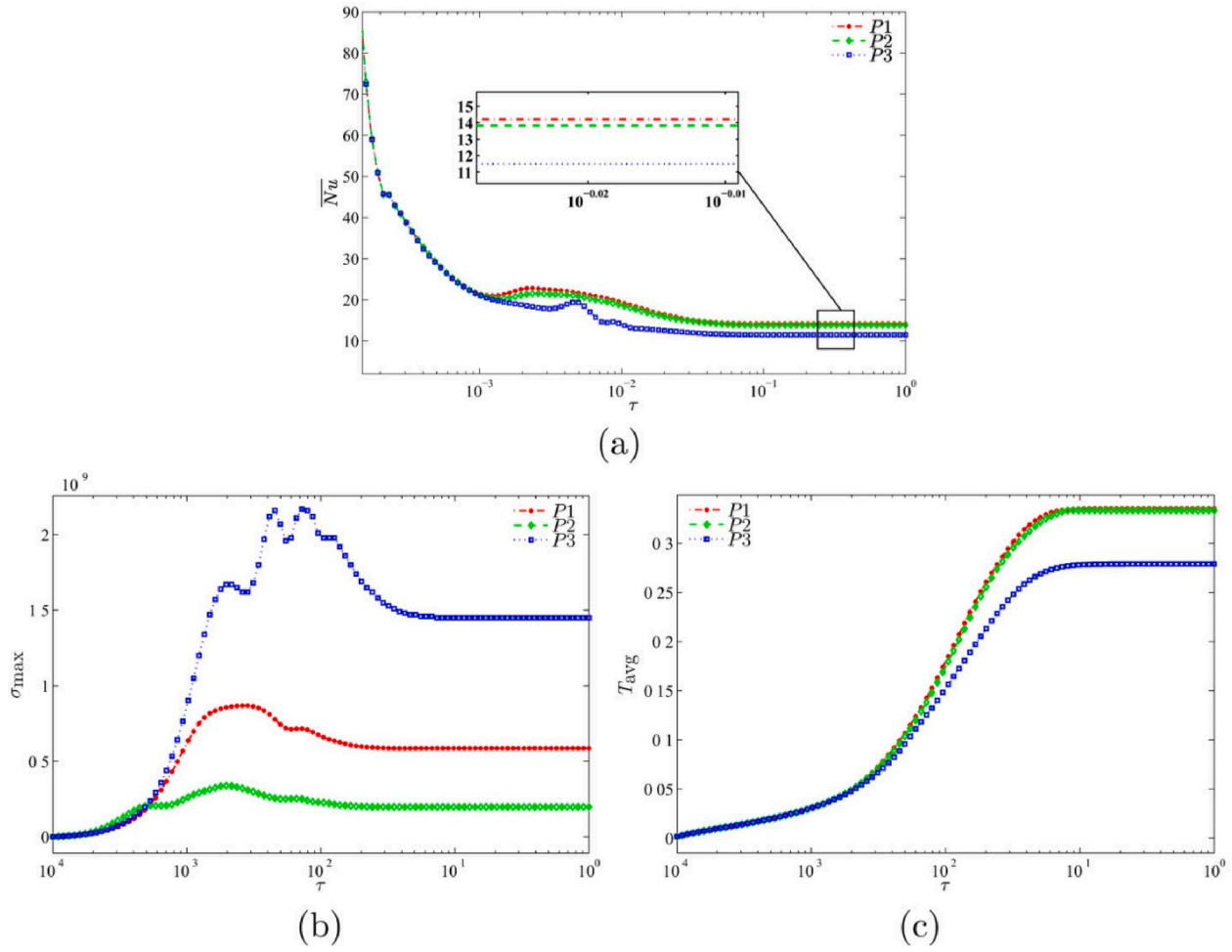

Fig. 14. Variations of the unsteady (a) average Nusselt number, (b) maximum stress on the flexible plate and (c) dimensionless temperature with τ for various fixed point locations ($P1$–$P3$) at $Ra = 10^6$, $\gamma = 45°$, $Pr = 6.2$, and $E = 5 \times 10^{10}$.

The effect of Rayleigh number on the fluid streams and the temperature fields are depicted in Fig. 10 for fixed point $P1$ at $\gamma = 90°$, $Pr = 6.2$, and $E = 5 \times 10^{10}$. At $Ra = 10^4$ and 10^5, the natural convection is weak, and the streamlines are symmetrically aligned in single weak circulations on two sides of the hot plate. Conduction is the primary heat transfer mechanism at low Rayleigh numbers. As the Rayleigh number increases, which means increasing the buoyancy force, natural convection becomes the dominant heat transfer mechanism. For $Ra = 10^6$, streamlines are stronger, which leads to the formation of two sub-vortices on each side of the cavity.

At low Ra, the isotherms are parallel to the vertical walls of the cavity, and a deviation of the isotherms from vertical states to horizontal states can be observed by increasing the Ra. Fig. 10 also illustrates that the thermal boundary layer around the plate is squeezed as the Ra increases. These indicate that the buoyancy-driven flow is becoming the main heat transfer mechanism in the cavity, and the thermal performance increases with increasing the Rayleigh number.

Fig. 11 illustrates the steady-state streamlines and isothermal contours for different inclination angles when the $P1$ is fixed for $Ra = 10^6$, $Pr = 6.2$, and $E = 5 \times 10^{10}$. The study is conducted for four different inclinations of the plate ($\gamma = 0°$, $30°$, $45°$, and $90°$). As the angle increases, the fluid circulation on the left and right sides of the cavity becomes more symmetric, and secondary vortices start to appear. At $\gamma = 0°$, the density of the streamlines is low at the bottom of the cavity, and hence, the low fluid motion is evident, and the isotherms are more separated from each other. This occurs due to the fact that when the plate is mounted horizontally, the flow movement should overcome the plate resistance to reach the bottom of the cavity. On the other hand, when the plate is mounted vertically, there is no resistance in the pathway of the flow to obstruct the flow movement of reaching the bottom of the cavity.

The variations of streamlines and isothermal contours are illustrated in Fig. 12 for three different Prandtl numbers ($Pr = 0.71$ (air), 6.2 (water) and 13.4 (seawater)), at fixed point $P1$ for $Ra = 10^6$, $\gamma = 90°$ and $E = 5 \times 10^{10}$. The streamlines and isothermal contours inside the enclosure have almost similar behavior at different Pr numbers. At $Pr = 0.71$, two circular streamlines are formed on the left and right sides of the plate. At $Pr = 6.2$, the main vortexes on each side of the plate break up into two double circular streams and the flow circulates in a double-eye motion on each side of the enclosure. For further increase of Pr, the two sub-vortices combine.

The variations of streamlines and isothermal contours are illustrated in Fig. 13 for different plate stiffness (elasticity modulus) (E), at fixed point $P1$ for $Ra = 10^6$, $\gamma = 90°$, and $Pr = 6.2$. As it can be observed, a fin with a very high value of elasticity modulus does not bend due to interaction with the fluid inside the cavity. By reducing the magnitude of the elasticity modulus, the plate starts to bend. The case with elasticity modulus of $E = 10^{13}$ or higher can be considered as a rigid plate. A slight bending can be noted in the case of $E = 10^{12}$. For the case of $E = 10^9$, the plate cannot resist the fluid-structure interaction and completely bend with the fluid. As seen, a complete bending of the plate has affected the streamlines and isotherms in the cavity.

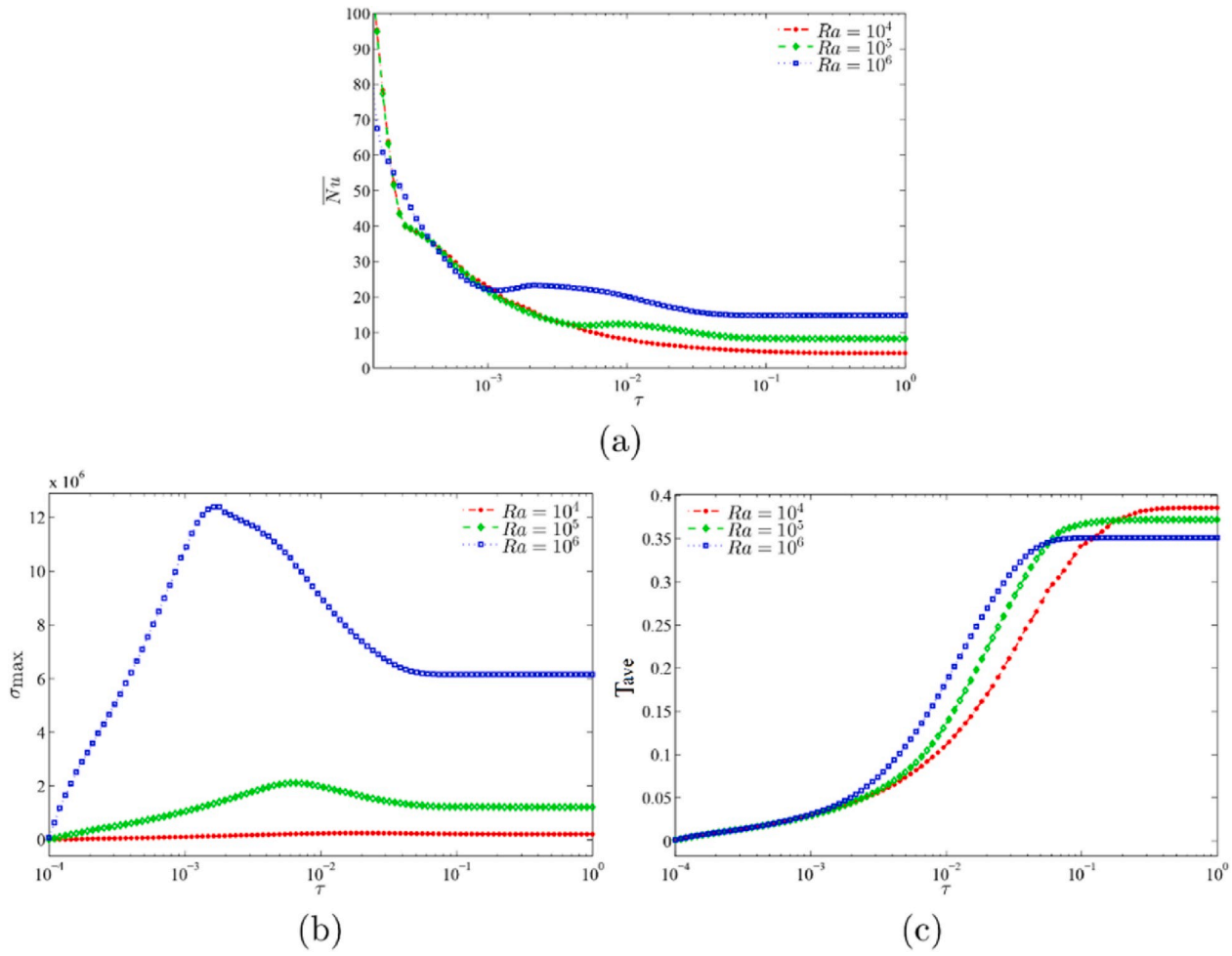

Fig. 15. Variations of the unsteady (a) average Nusselt number, (b) maximum stress on the flexible plate and (c) dimensionless temperature with τ for various Ra at fixed point 1 ($P1$), $\gamma = 90°$, $Pr = 6.2$, and $E = 5 \times 10^{10}$.

Average Nusselt number ($\overline{Nu}$), the maximum stress on the plate (σ_{max}), and the average temperature of the fluid flowing in the cavity (T_{avg}) are illustrated in Fig. 14 as a function of dimensionless time for fixed points $P1$–$P3$ for $Ra = 10^6$, $\gamma = 45°$, $Pr = 6.2$ and $E = 5 \times 10^{10}$. Initially, very high average Nusselt numbers were calculated, which is associated with a high-temperature difference between the plate and the fluid. As time elapses, the average Nusselt number for three different fixed points decreases and reaches the steady-state condition at about $\tau = 10^{-1}$ (see Fig. 14 (a)). Considering that $\overline{Nu}$ serves as a measure of the heat transfer inside the cavity, the heat transfer decreases as the fixed point moves higher.

Variation of the unsteady maximum stress on the plate for three different fixed points is illustrated in Fig. 14 (b). Tension on the plate peaks during the transition time for all the three fixed points. The plate experiences the highest stress and consequently the most deformation when it is fixed at $P3$. At the steady-state condition ($\tau > 0.01$), the maximum stress on the thin plate fixed at $P3$, is about six times higher than σ_{max} for $P2$. The plate deformation is shown in Fig. 9 also confirms that the maximum stress at the thin heater plate is lower at $P2$. Results in Fig. 14 (c) indicate that the steady-state average temperature is lower for fixed point $P3$ comparing with fixed points at $P1$ or $P2$.

Average Nusselt number, maximum stress on the hot plate, and average temperature in the cavity are plotted as a function of non-dimensional time in Fig. 15 for different Rayleigh numbers at fixed point $P1$, $\gamma = 90°$, and $E = 5 \times 10^{10}$. As shown in Fig. 15 (a), the average Nusselt number declines over time in the transient process for all Rayleigh numbers and eventually levels off in the steady-state situation. It can be seen that the Nusselt number and consequently, the heat transfer in the enclosure decreases with the reduction of Rayleigh number.

For $Ra = 10^4$, where the conduction is the dominant mechanism of heat transfer, the maximum stress on the hot plate does not change significantly and the order of its magnitude remains constant at 10^4. At $Ra = 10^5$, maximum stress on the hot plate starts from zero and reaches its highest value at $10^{-3} < \tau < 10^{-2}$. Then, it slightly decreases to reach the steady-state situation as time passes. For further increase in Rayleigh number, the natural convection dominates the heat transfer in the cavity, and σ_{max} increases significantly, as shown in Fig. 15 (b). It is interesting to mention that in the transition time, the average temperature in the cavity has the lowest value for $Ra = 10^4$. In contrast, in the steady-state condition, the higher temperature is related to a smaller Rayleigh number (Fig. 15 (c)).

The effect of the inclination angle of the plate on the heat transfer and fluid flow is illustrated in Fig. 16. As shown in Fig. 16 (a), The average Nusselt number increases slightly as the inclination angle increases. For all values of γ, the maximum stress increases in the transition time and reaches its highest values before leveling off in the steady-state condition. The maximum stress on the plate for $\gamma = 90°$ at $P1$, which is also presented in Fig. 15, can be neglected when compared with the higher-order results shown in Fig. 16 for lower values of γ. This was expected due to the symmetry of the streamlines in the left and right sides of the cavity observed in Figs. 7 and 10. Moreover, the average

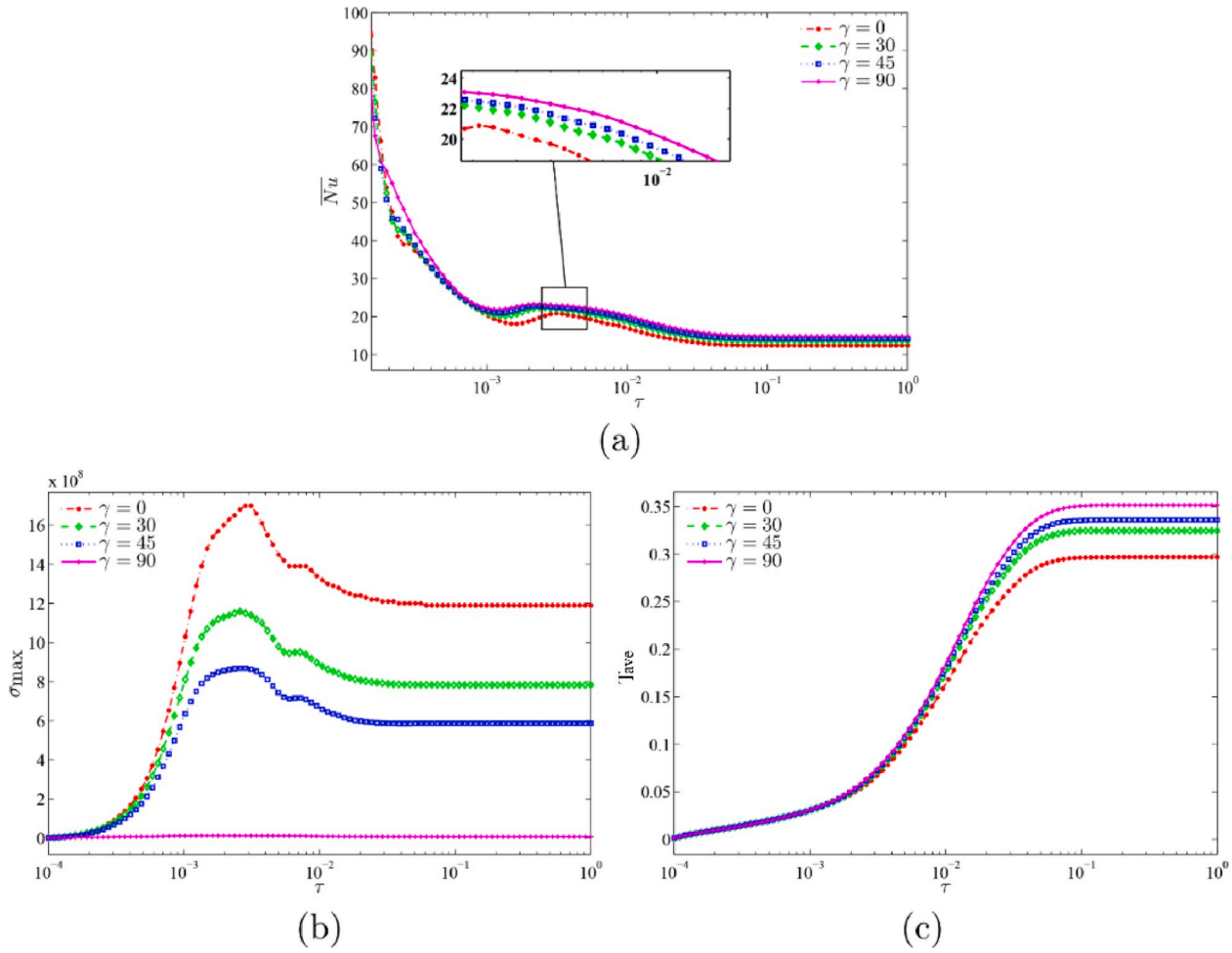

Fig. 16. Variations of the unsteady (a) average Nusselt number, (b) maximum stress on the flexible plate and (c) dimensionless temperature with τ for various γ at fixed point 1 ($P1$), $Ra = 10^6$, $Pr = 6.2$, and $E = 5 \times 10^{10}$.

temperature increase with increasing the inclination angle of the plate.

Variations of the unsteady $\overline{Nu}$, σ_{max} and T_{avg} are plotted in Fig. 17 for different values of Prandtl number (Pr). The effect of Prandtl number on average Nusselt number and average temperature on the steady-state situation is so small that it can be neglected. The maximum stress on the hot plate when air is the working fluid ($Pr = 0.71$) is small, with minor changes in the transient state. The plate is exposed to higher tensions by increasing the Pr. The increase of viscous forces tends to reduce the flow circulation while the increase of the buoyancy forces tends to raise the flow circulation. Hence, as the Pr contributes to the viscous terms as well as the buoyancy forces, the increase of the Pr in liquids has a minimal effect on the fluid circulation and its hydraulic for liquids. The maximum tensions in the plate, σ_{max}, for seawater ($Pr = 13.4$) is about two times higher than when water ($Pr = 6.2$) is used as the working fluid in the cavity.

Fig. 18 depicts the steady-state average Nusselt number and maximum stress on the hot plate for different fixed points in a wide range of inclination angles. As γ increases, the average Nusselt number rises consistently for fixed points $P1$ and $P2$ while the trend is opposite for $P3$ in $0° < \gamma < 40°$. The average Nusselt number for the fixed point at $P3$ experiences its lowest value at $\gamma \approx 40°$, and for higher inclination angles increases, significantly. The average Nusselt number and the heat transfer in the cavity are equal for all the fixed points at $\gamma = 90°$. The maximum tension on the flexible hot plate declines almost linearly by increasing the slope of the plate at fixed points $P1$ and $P2$, while the trend is different for fixed-point $P3$. In Fig. 18 (b), the highest stress occurs when the hot plate is fixed at $P3$ with $\gamma \approx 40°$.

Fig. 19 illustrates the steady-state changes of the average Nusselt number and maximum stress for different inclination angles at $P1$ as a function of Rayleigh number. As Ra increases, convection dominates the heat transfer mechanism in the cavity, and it increases the average Nusselt number. Unlike the case where the plate is fixed at $P3$, shown in Fig. 18 (a), the average Nusselt number increases with increasing the γ for all $Ra > 10^4$ at $P1$. As expressed before and can be seen in Fig. 19 (b), the maximum tension induced to the flexible plate is small for all the Ra when the inclination angle is 90°. For lower angles, the flexible plate tolerates more stress, and the maximum occurs at $\gamma = 0°$. As seen, the increase of the Rayleigh number boosts the effect of inclination angle on the average Nusselt number, maximum stress, and the free tip deflection of the hot plate. Indeed, the increase of the Ra intensifies the buoyancy forces and consequently, the flow circulation in the cavity. As the flow strength increases, the interaction of the fluid and solid boosts. A strong interaction of the fluid and structure leads to high values of the stress field and structure displacement. Moreover, when the flow circulations are stronger (the case of high values of the Ra) the change of inclination angles, which changes the flow hydrodynamic of the cavity, is much evident.

Fig. 20 presents the changes in the average Nusselt number, maximum stress, and free tip displacement of the plate for different values of Pr as a function of the inclination angle at fixed point 1 for $Ra = 10^6$. A higher Prandtl number results in a higher average Nusselt number for all values of γ. The grow of the inclination angle from 0° to

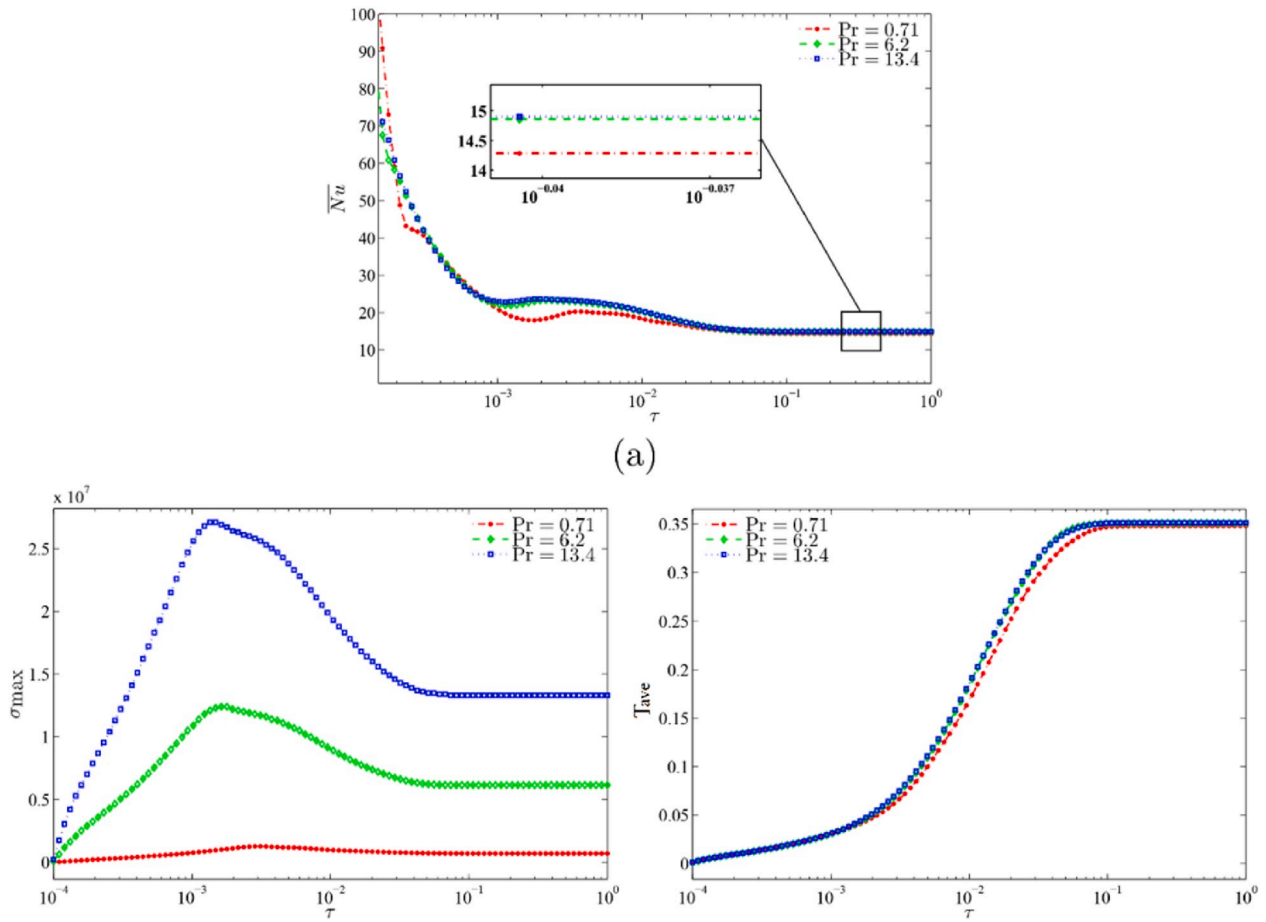

Fig. 17. Variations of the unsteady (a) average Nusselt number, (b) maximum stress on the flexible plate and (c) dimensionless temperature with τ for various *Pr* at fixed point 1 (*P*1), $Ra = 10^6$, $\gamma = 90^\circ$, and $E = 5 \times 10^{10}$.

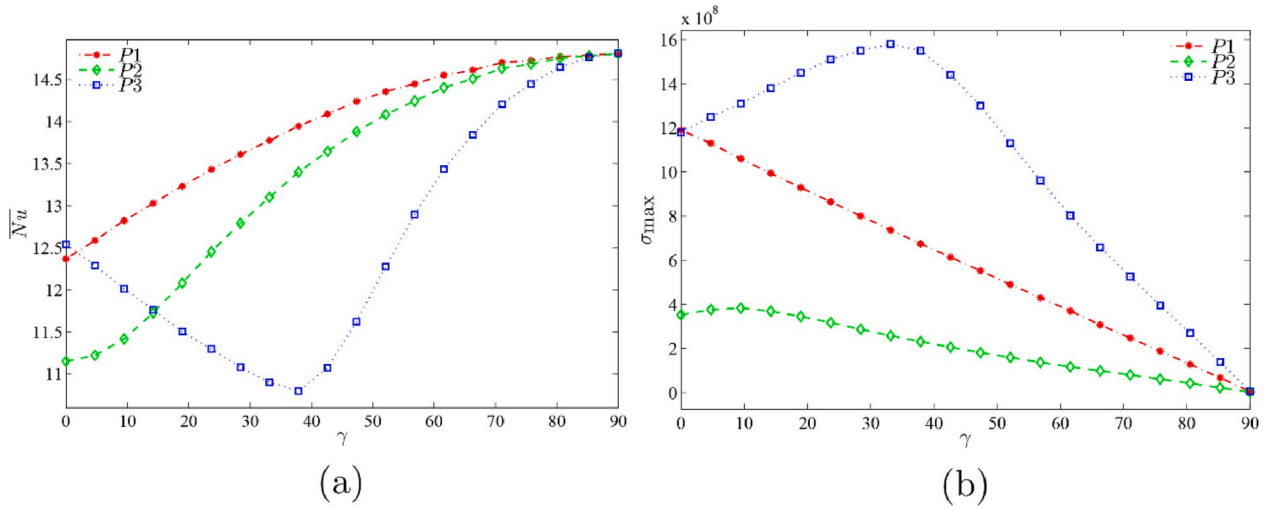

Fig. 18. Variations of the steady-state (a) average Nusselt number, and (b) maximum stress on the flexible plate with γ for various fixed point locations *P*1–*P*3 at $Ra = 10^6$, $Pr = 6.2$, and $E = 5 \times 10^{10}$.

90° rises the average Nusselt number for all Prandtl numbers. Hence, increasing the slope of the plate and also using a fluid with a higher Prandtl number can result in a higher heat transfer in the cavity. Based on Fig. 20 (b), the maximum stress on the flexible thin plate fixed at *P*1 occurs when the inclination angle is zero and $Pr = 13.4$. At lower inclination angles, the *Pr* has more effects on the maximum stress induced on the plate.

The increase of the inclination angle contributes to the hydrodynamic behavior of the fluid inside the cavity by reducing the flow resistance. An inclined plate allows the flow to circulate inside the cavity easily. Hence, as seen, the increase of the inclination angle improves the heat transfer. As an inclined plate reduces the drag on the fluid and eases

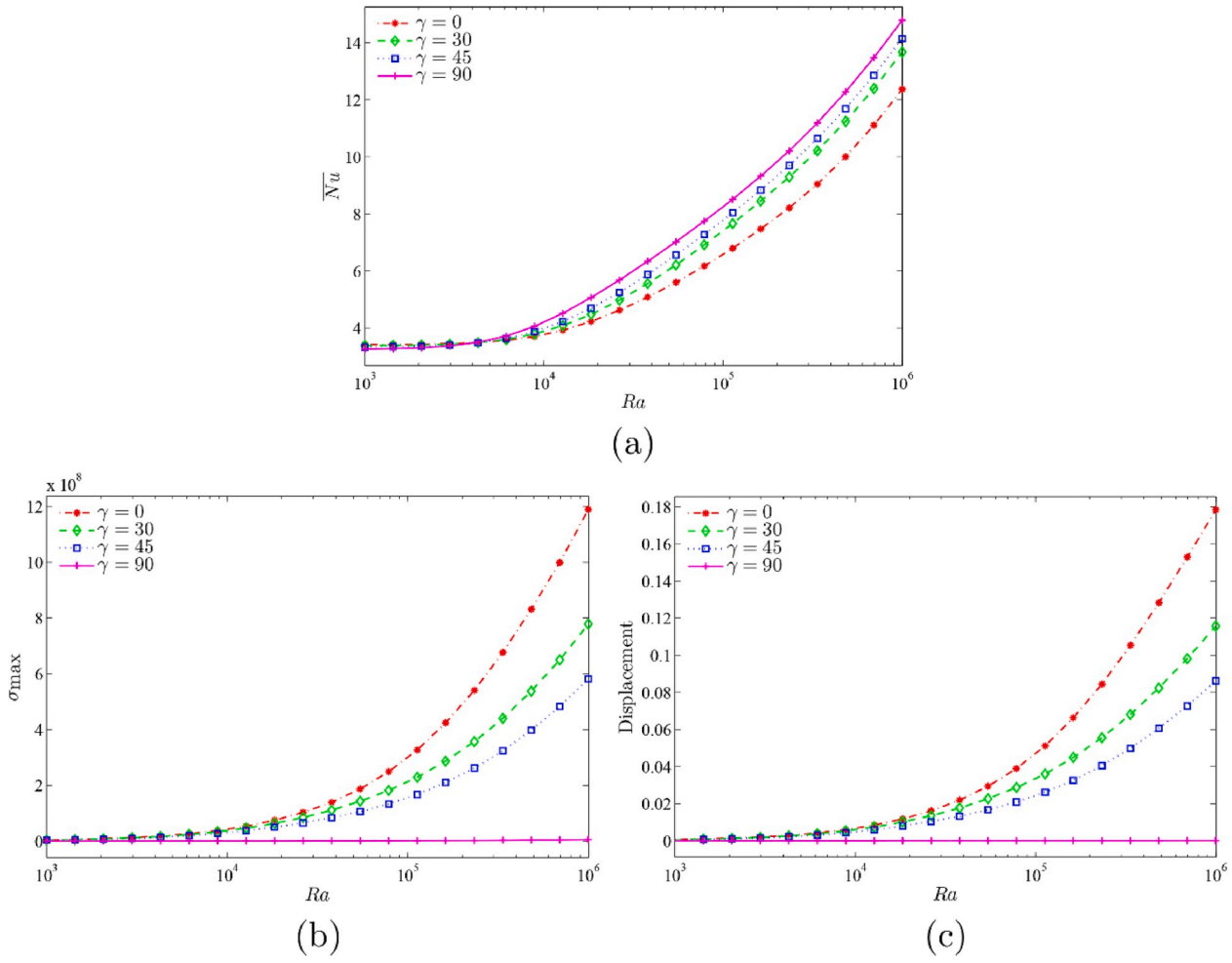

Fig. 19. Variations of the steady (a) average Nusselt number, (b) maximum stress on the flexible plate and (c) displacement at the free end of the flexible plate with Ra for various γ at fixed point 1 ($P1$), $Pr = 6.2$, and $E = 5 \times 10^{10}$.

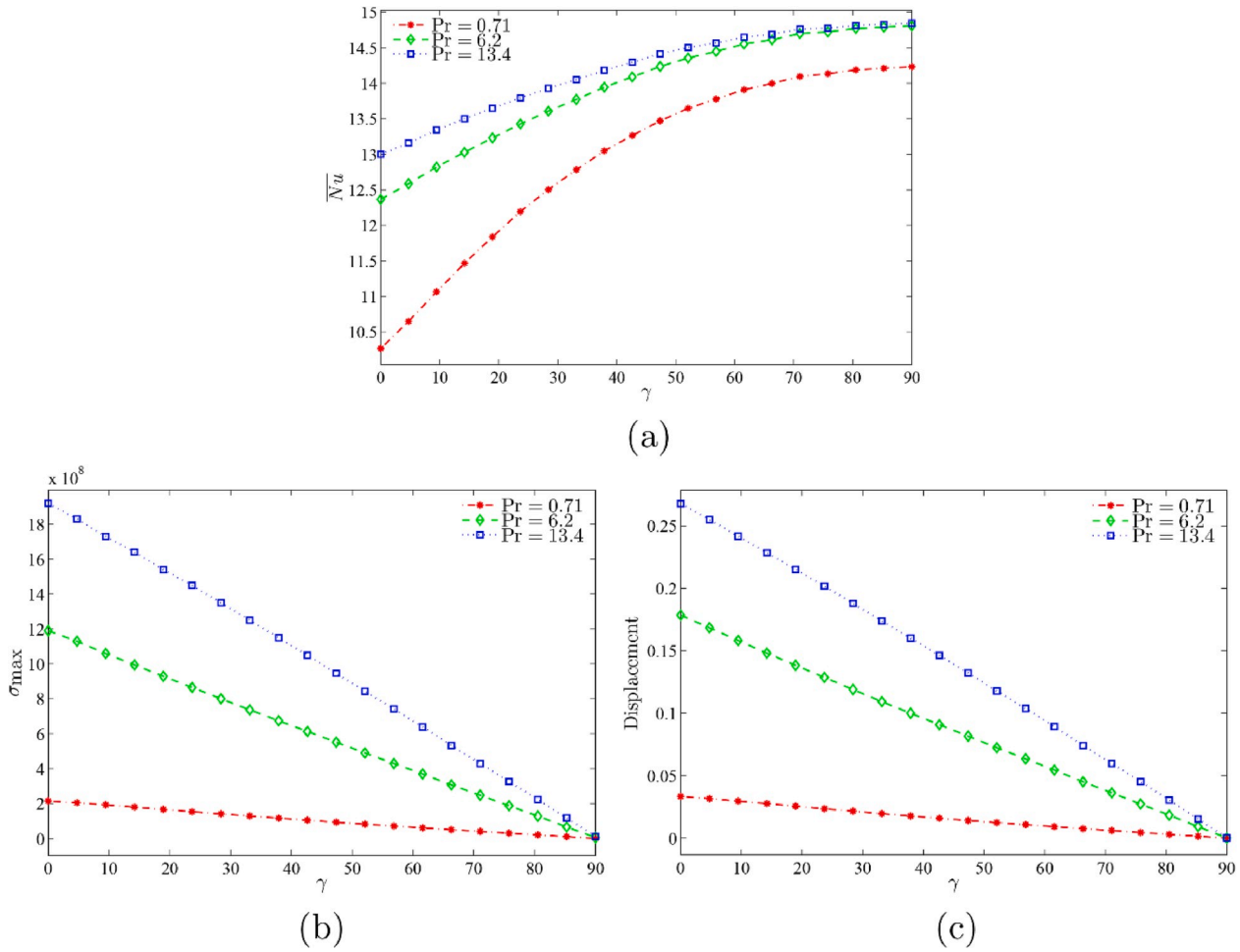

Fig. 20. Variations of the steady (a) average Nusselt number, (b) maximum stress on the flexible plate and (c) displacement at the free end of the flexible plate with γ for various Pr at fixed point 1 ($P1$), $Ra = 10^6$, and $E = 5 \times 10^{10}$.

the fluid circulation, the maximum tensions, and the tip displacement are also a declining function of the inclination angle.

The length of the plate can be changed during its deformation. For instance, a plate with an initial non-dimensional length of 0.4 (fixed at $P1$, an inclination angle of 45°, and $E = 10^{10}$) shows an ultimate increase of 0.82% of length at its stretching side and 0.79% decrease of length at the shrinking side. As the plate is very thin, the difference between the change of the length of the plate at the stretching and the shrinking sides is minimal. Here, the net increase in the length of the plate is 0.03%. This tiny net increase of the length of the plate, which contributes to the heat transfer from the plate, is about the order of mesh sizes. Hence, it cannot be a reason for the notable variation of the Nusselt number after the deflection of the plate.

The variation of the average Nusselt number, maximum value of stress on the plate and displacement at the free end of the plate are illustrated in Fig. 21 for the following range of parameters: $10^3 \leq Ra \leq 10^6$, and $10^9 \leq E \leq 10^{14}$. Here, the plate with $E = 10^{14}$ is considered as a rigid plate with no flexibility. Fig. 21 (a) shows that in the range of $Ra = 10^3$–10^4, the value of the average Nusselt number does not change significantly as a function of the plate's flexibility. As the Ra increases, the heat transfer increases more for lower elasticity modulus. Therefore, a flexible plate induces higher heat transfer at higher Ra.

Fig. 21 (b) present the effect of elasticity modulus on the maximum value of the stress on the plate in the steady-state situation. At the low range of Ra (10^3–10^4), the flexibility of the plate does not have a noticeable impact on σ_{max}, while at higher Ra, by increasing the stiffness of the flexible plate, the stresses inside the plate notably elevate. As a comparison, it can be seen that at $Ra = 10^6$, σ_{max} for the stiffest case ($E = 10^{14}$), is almost eight times higher compared to the most flexible plate ($E = 10^9$). The variation of the displacement at the free end of the flexible plate is illustrated in Fig. 21 (c) as a function of Ra for different values of elasticity modulus. This figure shows that for $E = 10^{14}$, the displacement at the free end of the plate is not influenced by the presence of the fluid, while by increasing the flexibility of the plate, higher displacement can be observed. Similar results are reported in Fig. 13 for plates with different flexibilities fixed at $P1$ at $Ra = 10^6$, $\gamma = 45°$ and $Pr = 6.2$.

A stiff plate shows higher maximum stresses as it resists to the flow interaction, and it undergoes small deflections. The deflection of the plate, along with the flow, reduces the interaction of the plate with the fluid and improves the hydrodynamic shape of the plate. Hence, a flexible plate shows lower tensions compared to a rigid plate.

5. Conclusion

Natural convection heat transfer in a 2D square cavity with a flexible hot plate in the center was studied numerically for different pertinent parameters. The plate is considered as an elastic body which undergoes large deformations, hence the fluid-structure interaction analysis was required to include the deformation of the plate. Vertical bonds of the wall were kept at a constant temperature, and the horizontal walls were adiabatic. The isothermal hot plate was fixed at one point (each end or the center of the plate) with different inclination angles with respect to the horizontal line. The results are discussed in terms of Nusselt number,

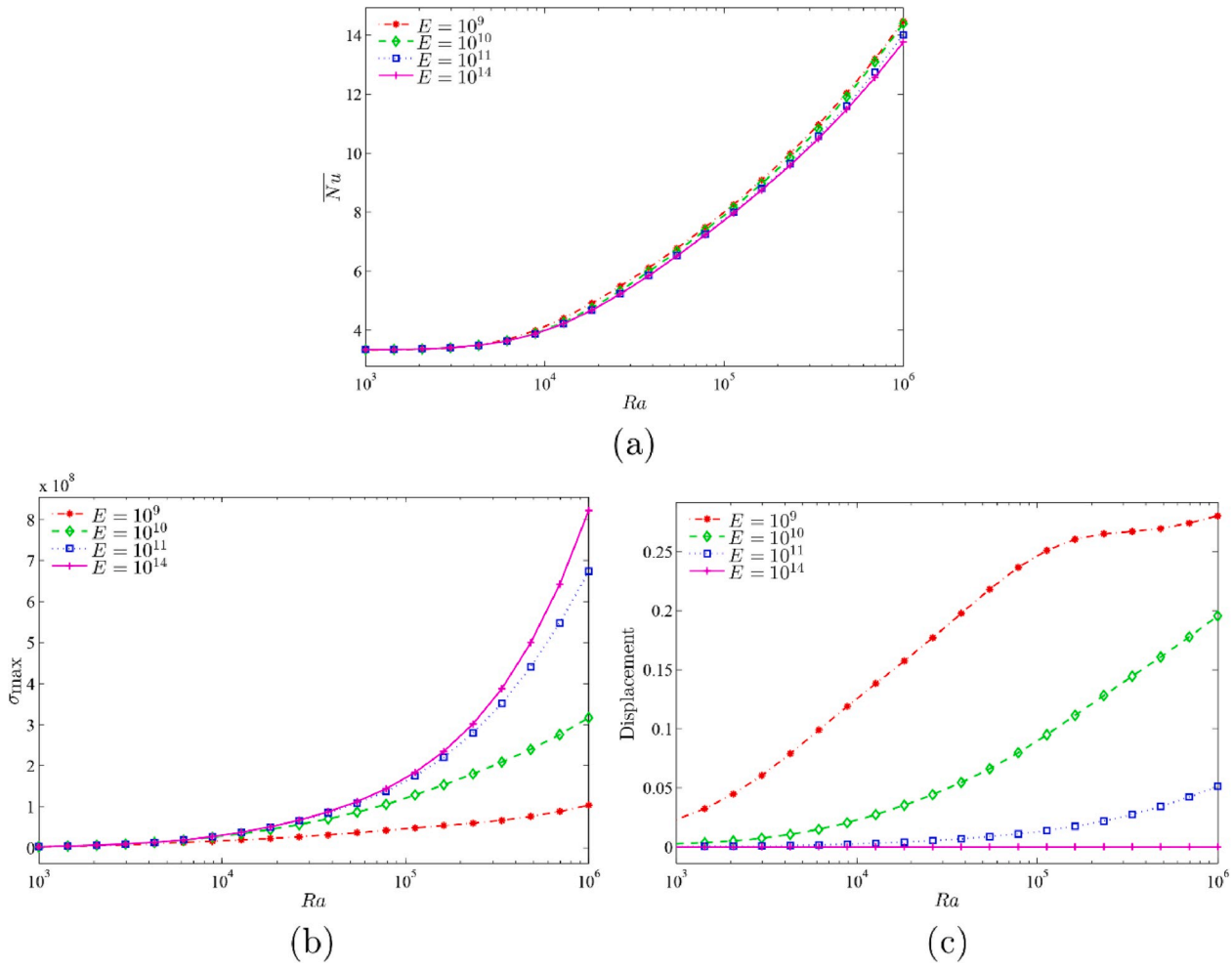

Fig. 21. Variations of the steady (a) average Nusselt number, (b) maximum stress on the flexible plate and (c) displacement at the free end of the flexible plate with Ra for various E at fixed point 1 ($P1$), $Ra = 10^6$ and $Pr = 6.2$.

Maximum stress on the plate, free tip displacement of the plate, and the average temperature plots as well as isotherms and streamline contours. The numerical results lead to the following conclusions:

- The location of the fixed point and the inclination angle significantly affect the heat transfer and fluid motion inside the cavity.
- The flexible plate experiences the lowest deformation and tension when fixed at its center ($P2$).
- The maximum stress on the flexible plate and its deformation are minimal at $\gamma = 90^\circ$ for all fixed points, at different Ra, and Pr numbers.
- For the fixed-points of $P1$ and $P2$, decreasing the inclination leads to a considerable increase in the maximum value of the stress on the hot plate and the maximum stress occurred when $\gamma = 0^\circ$, while $\gamma \approx 40^\circ$ is the critical inclination angle with a peak tension and minimum average Nusselt number when the plate is fixed at $P3$.
- When the fixed point is $P1$ and $Ra = 10^6$, $\gamma = 45^\circ$ and $Pr = 6.2$, the increase of the flexibility of the plate increases the heat transfer and reduces the internal tensions in the plate. However, a flexible plate shows larger deformations. As a result, a flexible plate shows a better heat transfer compared to a rigid plate.

Declaration of competing interest

The authors clarify that there is no conflict of interest for report.

Appendix A. Supplementary data

Supplementary data to this article can be found online at https://doi.org/10.1016/j.ijthermalsci.2020.106340.

References

[1] A. Al-Amiri, K. Khanafer, J. Bull, I. Pop, Effect of sinusoidal wavy bottom surface on mixed convection heat transfer in a lid-driven cavity, Int. J. Heat Mass Tran. 50 (2007) 1771–1780.
[2] M. Rahman, H.F. Öztop, A. Ahsan, M. Kalam, Y. Varol, Double-diffusive natural convection in a triangular solar collector, Int. Commun. Heat Mass Tran. 39 (2012) 264–269.
[3] S. Lorente, A. Bejan, J. Niu, Phase change heat storage in an enclosure with vertical pipe in the center, Int. J. Heat Mass Tran. 72 (2014) 329–335.
[4] F. Garoosi, F. Hoseininejad, M.M. Rashidi, Numerical study of natural convection heat transfer in a heat exchanger filled with nanofluids, Energy 109 (2016) 664–678.
[5] S. Yarmohammadi, K. Mohammadzadeh, M. Farhadi, H. Hajimiri, A. Modir, Multi-objective optimization of thermal and flow characteristics of R-404A evaporation through corrugated tubes, J. Energy Storag. 27 (2020), 101137.
[6] W. Zhang, Y. Wei, X. Chen, H.-S. Dou, Z. Zhu, Partitioning effect on natural convection in a circular enclosure with an asymmetrically placed inclined plate, Int. Commun. Heat Mass Tran. 90 (2018) 11–22.
[7] M.C. Ece, E. Büyük, Natural-convection flow under a magnetic field in an inclined rectangular enclosure heated and cooled on adjacent walls, Fluid Dynam. Res. 38 (2006) 564.
[8] Z. Altaç, Ö. Kurtul, Natural convection in tilted rectangular enclosures with a vertically situated hot plate inside, Appl. Therm. Eng. 27 (2007) 1832–1840.
[9] T. Tayebi, A.J. Chamkha, Entropy generation analysis during MHD natural convection flow of hybrid nanofluid in a square cavity containing a corrugated conducting block, Int. J. Numer. Methods Heat Fluid Flow 30 (3) (2019) 1118–1136.

[10] T. Tayebi, A.J. Chamkha, M. Djezzar, Natural convection of CNT-water nanofluid in an annular space between confocal elliptic cylinders with constant heat flux on inner wall, Sci. Iran. 26 (2019) 2770–2783.
[11] M. Ghalambaz, A. Doostani, E. Izadpanahi, A.J. Chamkha, Conjugate natural convection flow of Ag–MgO/water hybrid nanofluid in a square cavity, J. Therm. Anal. Calorim. (2019) 1–16.
[12] M. Ghalambaz, A.J. Chamkha, D. Wen, Natural convective flow and heat transfer of Nano-Encapsulated Phase Change Materials (NEPCMs) in a cavity, Int. J. Heat Mass Tran. 138 (2019) 738–749.
[13] A. Hajjar, S. Mehryan, M. Ghalambaz, Time periodic natural convection heat transfer in a nano-encapsulated phase-change suspension, Int. J. Mech. Sci. 166 (2020), 105243.
[14] S. Mehryan, M. Ghalambaz, L.S. Gargari, A. Hajjar, M. Sheremet, Natural convection flow of a suspension containing nano-encapsulated phase change particles in an eccentric annulus, J. Energy Storag. 28 (2020), 101236.
[15] M. Ghalambaz, A. Tahmasebi, A. Chamkha, D. Wen, Conjugate local thermal non-equilibrium heat transfer in a cavity filled with a porous medium: analysis of the element location, Int. J. Heat Mass Tran. 138 (2019) 941–960.
[16] M. Hashemi-Tilehnoee, A. Dogonchi, S.M. Seyyedi, A.J. Chamkha, D. Ganji, Magnetohydrodynamic natural convection and entropy generation analyses inside a nanofluid-filled incinerator-shaped porous cavity with wavy heater block, J. Therm. Anal. Calorim. (2020) 1–13.
[17] Z. Rashed, S. Ahmed, M.A. Sheremet, MHD buoyancy flow of nanofluids over an inclined plate immersed in uniform porous medium in the presence of solar radiation, J. Mech. 35 (2019) 563–576.
[18] M. Ghalambaz, T. Groşan, I. Pop, Mixed convection boundary layer flow and heat transfer over a vertical plate embedded in a porous medium filled with a suspension of nano-encapsulated phase change materials, J. Mol. Liq. 293 (2019), 111432.
[19] A. Dogonchi, T. Tayebi, A.J. Chamkha, D. Ganji, Natural convection analysis in a square enclosure with a wavy circular heater under magnetic field and nanoparticles, J. Therm. Anal. Calorim. 139 (2020) 661–671.
[20] A.I. Alsabery, M.A. Ismael, A.J. Chamkha, I. Hashim, Effect of nonhomogeneous nanofluid model on transient natural convection in a non-Darcy porous cavity containing an inner solid body, Int. Commun. Heat Mass Tran. 110 (2020), 104442.
[21] Q. Wang, M. Yang, W. Tao, Natural convection in a square enclosure with an internal isolated vertical plate, Wärme-und Stoffübertragung 29 (1994) 161–169.
[22] X. Shi, J. Khodadadi, Laminar natural convection heat transfer in a differentially heated square cavity due to a thin fin on the hot wall, J. Heat Tran. 125 (2003) 624–634.
[23] A. Modir, M. Kahrom, A. Farshidianfar, Mass ratio effect on vortex induced vibration of a flexibly mounted circular cylinder, an experimental study, Int. J. Marine Energy 16 (2016) 1–11.
[24] A. Modir, N. Goudarzi, Experimental investigation of Reynolds number and spring stiffness effects on vortex induced vibrations of a rigid circular cylinder, Eur. J. Mech. B Fluid 74 (2019) 34–40.
[25] H. Golparvar, S. Irani, M.M. Sani, Experimental investigation of linear and nonlinear aeroelastic behavior of a cropped delta wing with store in low subsonic flow, J. Braz. Soc. Mech. Sci. Eng. 38 (2016) 1113–1130.
[26] M. Sayed, T. Lutz, E. Krämer, S. Shayegan, R. Wüchner, Aeroelastic analysis of 10 MW wind turbine using CFD–CSD explicit FSI-coupling approach, J. Fluid Struct. 87 (2019) 354–377.
[27] K. Khanafer, Comparison of flow and heat transfer characteristics in a lid-driven cavity between flexible and modified geometry of a heated bottom wall, Int. J. Heat Mass Tran. 78 (2014) 1032–1041.
[28] E. Jamesahar, M. Ghalambaz, A.J. Chamkha, Fluid–solid interaction in natural convection heat transfer in a square cavity with a perfectly thermal-conductive flexible diagonal partition, Int. J. Heat Mass Tran. 100 (2016) 303–319.
[29] M. Ghalambaz, S. Mehryan, M.A. Ismael, A. Chamkha, D. Wen, Fluid–structure interaction of free convection in a square cavity divided by a flexible membrane and subjected to sinusoidal temperature heating, Int. J. Numer. Methods Heat Fluid Flow (2019), https://doi.org/10.1108/HFF-12-2018-0826. In press.
[30] A. Alsabery, F. Selimefendigil, I. Hashim, A. Chamkha, M. Ghalambaz, Fluid-structure interaction analysis of entropy generation and mixed convection inside a cavity with flexible right wall and heated rotating cylinder, Int. J. Heat Mass Tran. 140 (2019) 331–345.
[31] A.I. Alsabery, H. Saleh, M. Ghalambaz, A.J. Chamkha, I. Hashim, Fluid-structure interaction analysis of transient convection heat transfer in a cavity containing inner solid cylinder and flexible right wall, Int. J. Numer. Methods Heat Fluid Flow 9 (2019) 3756–3780.
[32] E. Jamesahar, M. Sabour, M. Shahabadi, S. Mehryan, M. Ghalambaz, Mixed convection heat transfer of nanofluids in a cavity with two oscillating flexible fins: a Fluid-Structure Interaction (FSI) approach, Appl. Math. Model. 82 (2020) 72–90.
[33] H. Garg, A.K. Soti, R. Bhardwaj, Vortex-induced vibration of a cooled circular cylinder, Phys. Fluids 31 (2019) 83608.
[34] H. Wan, S.S. Patnaik, Suppression of vortex-induced vibration of a circular cylinder using thermal effects, Phys. Fluids 28 (2016), 123603.
[35] A. Al-Amiri, K. Khanafer, Fluid–structure interaction analysis of mixed convection heat transfer in a lid-driven cavity with a flexible bottom wall, Int. J. Heat Mass Tran. 54 (2011) 3826–3836.
[36] K. Khanafer, Fluid–structure interaction analysis of non-Darcian effects on natural convection in a porous enclosure, Int. J. Heat Mass Tran. 58 (2013) 382–394.
[37] M. Ghalambaz, E. Jamesahar, M.A. Ismael, A.J. Chamkha, Fluid-structure interaction study of natural convection heat transfer over a flexible oscillating fin in a square cavity, Int. J. Therm. Sci. 111 (2017) 256–273.
[38] S. Mehryan, M. Ghalambaz, M.A. Ismael, A.J. Chamkha, Analysis of fluid-solid interaction in MHD natural convection in a square cavity equally partitioned by a vertical flexible membrane, J. Magn. Magn Mater. 424 (2017) 161–173.
[39] S.M.H. Zadeh, S. Mehryan, E. Izadpanahi, M. Ghalambaz, Impacts of the flexibility of a thin heater plate on the natural convection heat transfer, Int. J. Therm. Sci. 145 (2019), 106001.
[40] Aurongzeb DM, Coolidge D, Thompson RC, inventors; Dell Products LP, assignee. Flexible heat spreader with differential thermal conductivity. United States patent US 10,088,878. 2018 Oct 2. https://patents.google.com/patent/US10088878B2/en.
[41] Qiu B, Guo X, Raupp JC, Ahrens M, Pidwerbecki D, Lofland SJ, Daskalakis GH, Yee SL, MacDonald M, inventors; Intel Corp, assignee. Flexible heat spreader. United States patent US 9,980,412. 2018 May 22. https://patents.google.com/patent/US9980412B2/en.
[42] Fletcher RD, Chen Y, inventors; Coolhead Tech Inc, assignee. Flexible heat exchangers for medical cooling and warming applications. United States patent US 7,077,858. 2006 Jul 18.https://patents.google.com/patent/US7077858B2/en.
[43] R.C. Sekol, T.J. Rinker, D. Chakraborty, J.A. Abell, Mechanically conformable micro-heat exchangers and methods for use in thermal management of target components, in: Google Patents, 2019.
[44] J.C. De Los Reyes, S. González Andrade, A combined BDF-semismooth Newton approach for time-dependent Bingham flow, Numer. Methods Part. Differ. Equ. 28 (2012) 834–860.
[45] O. Schenk, K. Gärtner, Solving unsymmetric sparse systems of linear equations with PARDISO, Future Generat. Comput. Syst. 20 (2004) 475–487.
[46] P. Wriggers, Nonlinear Finite Element Methods, Springer Science & Business Media, 2008.
[47] F. Verbosio, A. De Coninck, D. Kourounis, O. Schenk, Enhancing the scalability of selected inversion factorization algorithms in genomic prediction, J. Comput. Sci. 22 (2017) 99–108.
[48] C.W. Hirt, A.A. Amsden, J. Cook, An arbitrary Lagrangian-Eulerian computing method for all flow speeds, J. Comput. Phys. 14 (1974) 227–253.
[49] T.J. Hughes, W.K. Liu, T.K. Zimmermann, Lagrangian-Eulerian finite element formulation for incompressible viscous flows, Comput. Methods Appl. Mech. Eng. 29 (1981) 329–349.
[50] J.N. Reddy, D.K. Gartling, The finite element method in heat transfer and fluid dynamics, 3rd Edition, CRC Press Taylor & Francis Group, 2010. https://www.crcpress.com/The-Finite-Element-Method-in-Heat-Transfer-and-Fluid-Dynamics/Reddy-Gartling/p/book/9781420085983.
[51] M.h. Souli, D.J. Benson, Arbitrary Lagrangian Eulerian and Fluid-Structure Interaction: Numerical Simulation, John Wiley & Sons, 2013.
[52] U. Küttler, W.A. Wall, Fixed-point fluid–structure interaction solvers with dynamic relaxation, Comput. Mech. 43 (2008) 61–72.
[53] O. Turan, A. Sachdeva, N. Chakraborty, R.J. Poole, Laminar natural convection of power-law fluids in a square enclosure with differentially heated side walls subjected to constant temperatures, J. Non-Newtonian Fluid Mech. 166 (2011) 1049–1063.
[54] F. Xu, J.C. Patterson, C. Lei, Heat transfer through coupled thermal boundary layers induced by a suddenly generated temperature difference, Int. J. Heat Mass Tran. 52 (2009) 4966–4975.
[55] B. Calcagni, F. Marsili, M. Paroncini, Natural convective heat transfer in square enclosures heated from below, Appl. Therm. Eng. 25 (2005) 2522–2531.